On Understanding the Lives of Dead Stars: Supernova Remnant N103B, Radio Pulsar B1951+32, and the Rabbit

by

Joshua Marc Migliazzo

Bachelor of Science, Physics (2001)
University of Texas at Austin

Submitted to the Department of Physics
in partial fulfillment of the requirements for the degree of

Master of Science in Physics

at the

MASSACHUSETTS INSTITUTE OF TECHNOLOGY

February 2003

Author .....
Department of Physics
January 17, 2003

Certified by .....
Claude R. Canizares
Associate Provost and Bruno Rossi Professor of Physics
Thesis Supervisor

Accepted by .....
Thomas J. Greytak
Chairman, Department Committee on Graduate Students

On Understanding the Lives of Dead Stars: Supernova Remnant N103B, Radio Pulsar B1951+32, and the Rabbit

by

Joshua Marc Migliazzo

Submitted to the Department of Physics
on January 17, 2003, in partial fulfillment of the
requirements for the degree of
Master of Science in Physics

Abstract

Using the Chandra High Energy Transmission Grating Spectrometer, we observed the young Supernova Remnant N103B in the Large Magellanic Cloud as part of the Guaranteed Time Observation program. N103B has a small overall extent and shows substructure on arcsecond spatial scales. The spectrum, based on 116 ks of data, reveals unambiguous Mg, Ne, and O emission lines. Due to the elemental abundances, we are able to tentatively reject suggestions that N103B arose from a Type Ia supernova, in favor of the massive progenitor, core-collapse hypothesis indicated by earlier radio and optical studies, and by some recent X-ray results. We present our latest two-temperature shock and two-dimensional spatial-spectral modeling of the remnant. If the massive progenitor conclusion holds true, it would significantly changes previous conceptions of the young SNR population in the LMC.

Using the Very Large Array and the Pie Town antenna, we have measured the position of the radio pulsar B1951+32 relative to nearby background radio sources at four epochs between 1989 and 2000. These data show a clear motion for the pulsar of 25 ± 4 $milliarcsec\ yr^{-1}$ at a position angle $252^\circ \pm 7^\circ$ (north through east), corresponding to a transverse velocity 240 ± 40 $km\ s^{-1}$ for a distance to the source of 2 kpc. The measured direction of motion confirms that the pulsar is moving away from the center of its associated supernova remnant, the first time that such a result has been demonstrated. Independent of assumptions made about the pulsar birth-place, we show that the measured proper motion implies an age for the pulsar of 64 ± 18 kyr, somewhat less than its characteristic age of 107 kyr. This discrepancy can be explained if the initial spin period of the pulsar was $P_0 = 27 \pm 6$ ms.

Thesis Supervisor: Claude R. Canizares
Title: Associate Provost and Bruno Rossi Professor of Physics

For My Family

Acknowledgments

The *Chandra X-Ray Observatory* is operated for the National Aeronautics and Space Administration by the Smithsonian Astrophysical Observatory's *Chandra* X-Ray Center in Cambridge, Massachusetts. *Chandra* data included in this work was obtained through the Guaranteed Time Observers project. The National Radio Astronomy Observatory is a facility of the National Science Foundation, operated under cooperative agreement by Associated Universities, Inc. This research has made use of NASA's Astrophysics Data System and the Centre de Donneés astronomiques de Strasbourg.

J. M. M. acknowledges the support of the Massachusetts Institute of Technology through a Presidential Fellowship for graduate study in Physics. Partial support for this thesis was provided by NASA under *Chandra* High Energy Transmission Grating contracts NAS8-01129 and NAS8-38249.

J. M. M. should especially like to thank his advisor, Professor Claude R. Canizares, for his support and guidance throughout the author's time at the MIT Center for Space Research. Prof. B. M. Gaensler and Dr. D. Dewey played crucial and patient roles in helping me analyze and understand the science of the second and first parts of this thesis, respectfully. Dr. K. A. Flanagan and Miss A. Fredricks are recognized for their help and insights in the analysis of SNR N103B, as are Professors D. C. Backer and R. G. Strom and Drs. B. W. Stappers and E. van der Swaluw, for their aid with PSR B1951+32. Credit goes to Dr. R. S. Foster for initiating the radio observations. J. M. M. is grateful to all those at the *Chandra* X-Ray Center High Energy Grating group at MIT who played a role in the completion of this work.

The author thanks his loving and lovely wife, Sophie C. Migliazzo, for making great inroads upon the many editorial and grammatical errors during the drafting, and for her constant encouragement during the writing of this thesis and the research leading up to it.

Contents

List of Figures

List of Tables

Chapter 1

Introduction

Twinkle, twinkle, little star, How I wonder what you are. Up above the world so high, Like a diamond in the sky. Twinkle, twinkle, little star, How I wonder what you are!

When the blazing sun is gone, When he nothing shines upon, Then you show your little light, Twinkle, twinkle, all the night. Twinkle, twinkle, little star, How I wonder what you are!

- Children's Nursery Rhyme, by Jane Taylor, 1806

In 1967, Jocelyn Bell, a graduate student of astronomy at Cambridge University, set out to study the twinkling of stars. Rather, she was to study scintillation, the distortion of radio signals caused by ions in interplanetary space, which corresponds to the atmospheric disturbance that causes twinkling of stars in visible light. Using the Cambridge dipole array radio telescope, she instead discovered short, rapid, and regular pulsations of radio radiation, arriving exactly 1.3373011 seconds apart. A month of observations fixed the direction of the pulsations somewhere in the constellation Vulpecula, the Fox. At the time, however, the question of the physical source of the pulsations was puzzling, even for the wiliest *Vulpes vulpes*. A natural thought attributed the signal to intelligent, extraterrestrial life, and the source was dubbed LGM, Little Green Men. Announcement of the discovery was withheld pending further study.

Soon, other sources, with pulse periods of 0.253065, 1.187911, and 1.2737635 seconds, were discovered in wildly different directions of the sky, and within a decade over a hundred of such sources, renamed pulsating sources of radio, or pulsars, were known and catalogued.

1.1 Pulsars

As the signals were coming from such widely separated directions of space, it seemed unlikely intelligent life was the origin. Sending pulses over such a wide range of wavelengths would be wasteful of energy and not intelligent at all. Furthermore, no Doppler shift, expected from a signal sent from a body orbiting a star, was detected.

Scintillation effects, which delay radiation as a function of frequency and allow distances to be estimated, confirmed the pulsars' existence in our own Galaxy, from a few hundred to a couple thousand parsecs away. Due to the finite speed of light, the pulsars' pulse widths, as short as one-fortieth of a second, implied the size of the emitting region to be shorter than one-fortieth of a lightsecond, or 7500 kilometers. These constraints eliminated all stars but white dwarfs and the theoretically-predicted, but never observed, neutron stars. White dwarfs are old stars, with a mass less than 1.4 times that of the sun (1.4 $M_{\odot}$), that began as low-mass stars like our Sun and thermonuclearly burned all the hydrogen into helium and then helium into carbon in their core. White dwarfs lack the mass and, thus, the gravitational pressure to burn the carbon ash into heavier elements. Having already passed through the low-mass star red giant phase, and perhaps forming a planetary nebula, white dwarfs have nothing left to burn and can only cool and shrink to the point where their (extremely high) density is stabilized, and their weight supported by the electron degeneracy pressure derived from the Pauli Exclusion Principle of quantum mechanics. In this state, white dwarfs will slowly radiate heat away for billions of years until arriving at thermal equilibrium with their surroundings.

Neutron stars were stars hypothesized to exist by theoreticians shortly after the discovery of the neutron in 1932. For old stars with a certain minimum mass, later

calculated by Indian-American physicist Subrahmanyan Chandrasekhar to be 1.4 $M_{\odot}$, the gravitational pressure would exceed the electron degeneracy pressure, forcing the stars to shrink further and become even more dense; free electrons would react with protons, leaving only neutrons in the core of the stars. Eventually, a neutron degeneracy pressure would support neutron stars from complete collapse; although similar to white dwarfs, neutron stars are more massive, more dense, and smaller. At about two or three solar masses, gravity would overcome even the neutron degeneracy pressure, and such stars would completely collapse into black holes.

Pulsars must have some physical mechanism for producing the pulsations of radiation; three are conceivable: rotation about an axis, oscillations of the star in size and brightness, and orbiting another star. With such short pulsation periods, separation distances shorter than the star's radii preclude the orbital possibility for white dwarfs. Albert Einstein's general theory of relativity eliminates orbiting neutron stars as a mechanism, as it predicts a large increase in the orbital period over time that is not observed. Studies of red supergiants, Mira variables, RR Lyrae stars, and Cepheid variables have yielded a firm understanding of star oscillations, the period of which varies inversely to the square root of the density. Thus, white dwarfs would have an oscillation period of a couple tens of seconds, too long for pulsars, and the more dense neutron stars would oscillate every hundredth of a second, too quickly for pulsars, which leaves only rotation. For a white dwarf of one solar mass rotating at the required rate, the centripetal force would exceed the gravitational force, and the star would fly apart. Smaller and more massive neutron stars, however, have a greater gravitational force, and, with a smaller radius, experience a smaller centripetal force; such stars can rotate at the required speed. Whence, as the only feasible possibility, pulsars are thought to be rotating neutron stars.

What could create such a star? Long before the discovery of pulsars, Walter Baade and Fritz Zwicky suggested supernovae might form neutron stars.

1.2 Supernovae

In contrast to the low-mass stars that cool into white dwarfs, more massive stars, after burning the hydrogen and helium in their cores, expand into red supergiants. Due to greater temperatures and pressures, such stars fuse carbon nuclei into heavier elements like magnesium, iron, cobalt, and nickel. Undergoing shrinking and heating, eventually even the iron fuses endothermically, resulting in further shrinking, heating, and energy loss to iron fusion. This instability leads to catastrophic core collapse and results in a massive production of neutrinos, which exert a large force on the neutrino opaque outer layers, setting off shock waves, creating heavy elements, and destroying the star. This explosion, this violent ejection of the outer layers of the star even as the iron core continues to shrink and collapse, is called a supernova.

Five supernovae occurring in our Galaxy have been observed in the past millennium: the first recorded in 1006 A.D. in the constellation Lupus, one in 1054 A.D., observed by the Chinese in the constellation Taurus, one in 1181 A.D. in Cassiopeia, one in 1572 A.D., observed by Danish astronomer Tycho Brahe, also in Cassiopeia, and one in 1604 A.D., described by German astronomer Johannes Kepler and Italian philosopher Galileo Galilei in constellation Serpens. A sixth was possibly recorded by Englishman John Flamsteed in 1680 A.D., appearing in Cassiopeia; in any case he did not seem to think anything special of it, and catalogued it as a regular star. Although several fascinating ones, notably SN 1987a, have been observed recently in other galaxies, it seems we are overdue for one in the Milky Way.

Supernovae are tremendously bright. That of 1054 is known to have been visible to the naked eye for several weeks in broad daylight, and for over a year and a half at night. Releasing an enormous amount of mechanical energy (some 10^{51} ergs) in the kinetic expansion of ejecta and the thermal emission of light, supernovae can, at their peak, outshine the sum total of all other stars in the galaxy in which they reside. But all this mechanical energy, including the emitted photons, represents less than 1% of the total energy released in the explosion; most of the energy escapes as neutrinos. Thus, supernovae are extremely important contributors of energy to

their galaxies. As elements above lithium are only produced in stars, supernovae also play an important role in adding heavy elements to the interstellar medium, the same elements that are present in virtually every molecule in our bodies, from the oxygen we breathe to the calcium in our bones.

Baade and Zwicky were the first to recognize supernovae as a distinct class of objects, differing from common novae, in 1934. Zwicky eventually proposed five classes of supernovae, Types I, II, III, IV, and V. Today, several classification schemes exist, but there are now essentially only two major classes. The first is comprised of the supernovae created by the process described above, to wit: core collapse in a massive star. This class is further sub-divided into groups, which, for historic reasons, are named: Type Ib, the result of a massive, probably Wolf-Rayet or O star, stripped of its hydrogen outer layer before the catastrophe, Type Ic, like Type Ib, but whose progenitor is stripped of both its hydrogen and helium outer layers, and Type II, resulting from massive red supergiant, early B stars. In this thesis, the terms core collapse supernovae and Type II supernovae are henceforth to be used interchangeably to mean all supernovae of this major class, having massive stars as progenitors. The second major class differs in that the progenitor is not thought to be a massive star at all, but rather a carbon-oxygen white dwarf which slowly accretes matter until exceeding the Chandrasekhar mass and explosively deflagrating. This class is called Type Ia.

As massive stars evolve and die more quickly than the less massive, Sun-like stars that become white dwarfs, the ages of supernova progenitors and the populations of stars in which they are found are very different for the two major supernova classes. Therefore, the different progenitors and supernovae produce contrasting amounts of atomic elements on the different time-scales of galactic chemical evolution. Thus, studies of supernovae and supernova remnants, the luminous, gaseous nebulae left as a testament to the fiery death of stars, furnish information on a variety of astrophysical problems.

Particularly important is the frequency or rate of supernovae in galaxies, which affects the structure, kinematics, and composition of the interstellar medium, and

they can influence the evolution of the galaxy itself. Supernova rates directly affect the birthrates of pulsars, X-ray binaries, and, perhaps, black holes, as well as the cosmic-ray flux. Rates of nearby core-collapse supernova are predicted to affect the detection probability of gravity waves.

However, a complete understanding of observed supernovae is limited by poor statistics and uncertain positions for many recorded events. For most galaxies, and especially those classified as irregular, the available supernova data are so few that the study of overall rates is seriously hampered, indicating a need for an alternative approach. One such approach is to apply the statistics of supernova remnants in nearby galaxies.

Chapter 2

The Supernova Remnant N103B and the Large Magellanic Cloud

What tumbling cloud did you cleave,
yellow-eyed hawk of the mind,
last evening? that I, who had sat
Dumbfounded before a knave,
Should give to my friend,
a pretence of wit.

- William Butler Yeats, **The Hawk**

Over 180 supernova remnants (SNRs) are known in the Milky Way, and many of their properties have been studied [31]. The high interstellar extinction at optical and X-ray wavelengths, however, makes a complete and systematic study of the Galactic population impossible. Furthermore, large uncertainties in distances to the remnants compound the extinction problem and severely hinder analysis of the remnants and their environments.

It thus becomes imperative to observe SNRs in other galaxies. While most extragalatic surveys are too incomplete, studies of SNRs in the Large Magellanic Cloud (LMC) are very good and relatively complete, especially for young remnants, owing to the relatively small distances, and low internal extinctions.

2.1 The Large Magellanic Cloud

The Large Magellanic Cloud presents itself as a unique laboratory for studying supernova remnants and their physical and statistical properties. At a high enough Galactic latitude to avoid the high extinction that plagues Galactic objects, and small enough to assume a similar distance of 50 *kpc* to all LMC remnants [100], the irregular galaxy is still close enough to allow production of radio, optical, and, now, X-ray images in which small-scale structure may be resolved and studied. Excellent environmental data are also available, including catalogs of OB associations, luminous stars and [H II] regions, and surveys of neutral hydrogen and molecular CO, providing some understanding of local densities. The LMC is a simpler system than the Galaxy, lacking a well-defined halo or disk, and is well mixed by gas motions along the central bar [72]. Finally, there is a large population of 32 known supernova remnants [58, 59, 60]; considered with the eleven in the SMC, there are more SNRs in the Magellanic Clouds than the total number known in all other irregular galaxies.

In fact, the elemental abundances relative to iron in the LMC match those of the present local Interstellar Medium better than those of the Sun, implying some similarity between the star formation histories of the LMC and the present solar neighborhood, and important differences with the local interstellar medium four and a half billion years ago when the Sun was born [80].

Thus, there are differences to be considered when attempting to use the LMC to infer certain properties of our own Galaxy. For instance, the O/Fe ratio for the LMC is smaller than that for the Sun. This fact itself might be exploited to predict the ratio of SNe of Type Ia to SNe of Type II (N_{Ia}/N_{II}) at different times in galactic evolution. As O is mainly produced by SNe II, and Fe mainly be Type SNe Ia, an accurate determination of the O/Fe ratio may indicate the corresponding N_{Ia}/N_{II} [79, 81]. Eventually, comparisons between the properties of the LMC and Milky Way could provide information on the effect of stellar environments, such as the larger gas fraction of the LMC, upon SNe and SNRs. For the moment, estimates of the N_{Ia}/N_{II} ratio for the LMC range from 1/5 to 1/4 [93], and estimates of the ratio range

from 1/10 to 1/4 for the solar neighborhood [4, 61], depending on which elemental abundances are selected to derive the SN ratio.

Therefore, estimates of N_{Ia}/N_{II} disagree and SN ratios are not currently well-known. Furthermore, knowledge of the ratio does not yield absolute SN rates in galaxies, which are important in understanding galactic evolution and dynamics. Instead, individual studies of an SNR population in a galaxy are needed, which, by determining supernova type, can fix the absolute SN rate and thereby measure the N_{Ia}/N_{II} ratio directly, as well as provide a consistency check on nucleosynthesis models.

2.2 History of N103B

The fourth brightest X-ray SNR in the Large Magellanic Cloud, with an unabsorbed X-ray flux of 5.943×10^{-11} $ergs\ cm^{-2}\ s^{-1}$ from $0.3-10$ keV [50, 58], SNR N103B (SNR 0509-68.7, Figure B-1) is a natural target for individual study. The remnant was first identified as such by Mathewson and Clarke [57] based on its non-thermal emission in radio wavelengths and on its relative emission-line strengths of [S II] and Hα. N103B is similarly bright in the radio, with flux densities of 1.36 Jy at 408 MHz [58], 0.75 Jy at 843 MHz [64], 0.73 Jy at 1 GHz [19], and 0.29 Jy at 5 GHz [65], implying a mean spectral index of $\alpha = -0.67$, comparable to other shell-type remnants in the LMC.

The small (radius = 3 pc), young shell-like remnant, measuring some $30'' \times 30''$ in X-rays [49], sits on the north-eastern edge of the gigantic [H II] region N103. SNR N103B shows a high degree of correlation between its radio and X-ray maps [48] on large scales (but not on small scales [36]), in particular as regards an approximate threefold enhancement on its western side, closest to the [H II] region and, thus, most likely a result of density contrasts.

Prior to more recent studies, there were indications that N103B was associated with the star cluster NGC 1850 [16], from which the remnant is only 40 pc distant, and which is composed of an old core surrounded by younger, bluer stars. Such an association suggested N103B to be a short lived, massive-star remnant (Type

II, Ib, or Ic). Additionally, echelle data of the remnant show enhanced emission at the velocity of the local [H II] region (DEM 84). Abundances of N103B inferred from optical spectroscopy resembled those of SNR N63A and N49 [80], much larger, more evolved remnants in the LMC within the OB associations LH 83, and LH 53, respectively. Specifically, N103B contains several bright knots at optical wavelengths with common SNR emission lines: [O III] λ5007, [Ne III] λ3868, [Fe II] $\lambda\lambda$4244, 5332, [S II] $\lambda\lambda$6716, 6731, Hα, among others [17]. Radio luminosity comparisons with other SNRs in the LMC, which indicate N103B was most likely a massive core-collapse SN, argue that since N103B has 1/8 the radio luminosity and 1/5 the X-ray luminosity of LMC companion and Type II remnant N132D, comparable to their area ratio of 1/10, N103B is likely a younger version of the same, with an age of a few hundred years [19]. N103B might be expanding in a low density region swept out by neighboring stellar activity. This contrasts somewhat with LMC companion SNR 0519-690, a Type Ia remnant that is of comaparible size to N103B, but has only 1/2 the X-ray and 1/10 the radio luminosity. European X-Ray Observatory Satellite (EXOSAT) and re-analyzed *Einstein Observatory* data of N103B indicated a thermal origin for X-rays [85] with a temperature of 1.2 keV, an age estimate of approximately 600 to 1200 yr, and a high density inside and around the remnant.

ASCA results pointed to a much different type progenitor [37]. Nineteen kiloseconds of data showed a broad smooth blend of emission peaking around 1 keV, the result of unresolved iron *L*-shell lines, along with Kα emission from He-like silicon, sulfur, argon, and calcium. Overall, the spectrum resembled the *ASCA* spectra of 0509-67.5 and 0519-69.0, themselves suspected Type Ia SNRs [94]. Due to the lack of O, Ne, and Mg emission needed to fit the spectra with a Non-Equilibrium Ionization (NEI) model, N103B was re-cast as a Type Ia remnant based only upon *ASCA* data. This surprising conclusion led to a second *ASCA* observation of 100 ks, which detected a previously unknown Fe K blend near 6.5 keV [38].

XMM-Newton observed N103B shortly thereafter, however, making clear detections of O, Ne, and Mg lines [34]. Furthermore, fits of the spectrum with NEI and Collisional Ionisation Equilibrium (CIE) models and comparisions to various theoreti-

cal abundance predicitons strongly indicated a Type II (massive) progenitor, espically as regarded large O/Si, Ne/Si, and Mg/Si ratio values, and relatively small Fe/Si ratios. A lower age limit of 1200 yr was reported, as was evidence of recent (200 yr) shocks; plasma temperatures of 0.55, 0.65 and 3.5 keV were used in fitting the data.

While admiting that analysis of radial sturcture cannot conclusively arbitrate the issue, a recent analysis of *Chandra* ACIS observations of 40.8 ks upholds the surprising Type Ia reclassification by arguing the radial distribution of the ejecta and yields of intermediate mass species are more consistent with Type Ia events [49]. The resulting confusion surrounding the true nature of the progenitor has inspired continued investigation of its properties in the hope of resolving the apparent contradiction, not only to understand the remnant itself, but the young remnant population as a whole.

Chapter 3

N103B Observations and Analysis

The more I looked, I wondered more...
A remnant of uneasy light,
A flash of something over-bright!

- William Wordsworth, **The Matron of Jedborough**

As one of the brightest remnants in the LMC, N103B presents itself as a natural target for study by X-ray satellites. In view of the considerable debate concerning the progenitor of N103B, and the considerable importance of the answer to this question in determining the SNR population of the LMC as discussed above, we undertook to observe the remnant with the High-Energy Transmission Grating Spectrometer (HETGS) aboard the *Chandra X-Ray Observatory*, which possesses a unique capability to resolve and image line emission from extended sources to infer physical parameters. N130B is a good candidate for HETGS observations in that its overall extent is small, and with substructure on the scale of arcseconds, well-resolved images of the SNR are possible with *Chandra*. Moreover, as a relatively young remnant, it is known to emit at X-ray wavelengths well-suited to the energy range of the HETGS.

3.1 The *Chandra X-Ray Observatory* and High Energy Transmission Grating Spectrometer

The *Chandra X-Ray Observatory* was launched on July 23, 1999, as one of NASA's four "Great Observatories" fleet of satellites. Placed in a highly eccentric orbit, uninterrupted observations as long as 55 hours are possible. Photons are focused by four concentric, grazing incidence, paired Wolter-1 paraboloid/hyperboloid optics. When desired, the High-Energy Transmission Grating [13, 55] can be interposed directly behind this mirror assembly to disperse the X-rays according to wavelength and project spectra onto the focal plane where it is recorded by the ACIS-S CCD array. The HETG is actually an array of 336 gold micro-structure grating facets, each about 25 mm^2, composing two grating types, the Medium- and High-Energy Gratings (MEG and HEG, respectively), which are each optimized for efficiency at different energies, and which partially overlap in spectral coverage to provide continuous spectral coverage from $0.4 - 10$ keV (corresponding to 30 to 1.2 Å). The *Chandra* HEG has an effective collecting area of 25 cm^2, and the MEG has an effective collecting area of 70 cm^2, at 6.7 Å, the wavelength of the helium-like Si emission triplet. The HETGS has a maximum spectral resolution of $\mathrm{E}/\Delta\mathrm{E} = 100 - 1000$ for point sources; the Advanced CCD Imaging Spectrometer (ACIS) also provides moderate-energy resolution of the zeroth-order image, which can attain an angular resolution of 0.5 arcseconds over the spectral range. For extended sources, spatial and spectral information are mixed along the dispersion axis, complicating analysis and decreasing effective resolution. Spatial-spectral analysis is still possible, however, especially when distinct spectral lines exist which are not excessively blurred by Doppler shifts.

3.2 Observations

Chandra observations, consisting of 73.1, 25.4, and 17.4 ks exposures (*Chandra* Observation Identification # 1045, 2410, and 2416, respectively) centered on SNR N103B, were conducted on day 1, 2, and 3 of 2001 as part of the Guaranteed Time Ob-

servers program. The three observations, which are at essentially the same roll angle of 340 °.1, together total 116 ks of data, utilized the HETGS, and cover the energy band $0.4 - 10$ keV ($30 - 1.2$ Å) with energy resolutions of up to 1000. The dispersed spectrum is recorded by the Advanced CCD Imaging Spectrometer (ACIS-S), which on those days was working in a standard readout mode. The temperature of the detector was -120°C. Canizares *et al.* [12] give a complete description of the HETG, and further details may be found in the *Chandra* Proposers' guide and at **http://space.mit.edu/HETG** .

Due to the similar roll angles, the three observations are easily combined to form a single large 115.9 ks data set in which 80,293 Level 2, *i.e.,* cleaned and Charge Transfer Inefficiency (CTI) corrected, photons were detected.

3.3 Data Reduction

The data furnished by the *Chandra X-ray Center (CXC)* are Level 1 events, which include all the telemetered event grades. These data were then reprocessed with the standard `CIAO` software package, version `R4CU5UPD13.2`, on November 30, 2001. First, the data were corrected with the tool `acis_process_events.csh`, which limits CTI degradation that occurs with the loss of charge in a CCD as it is shifted from one pixel to the next during detector readout. Due to proton damage early in the mission, *Chandra*'s detector has a greatly increased susceptibility to CTI effects, which change the grade of events, making good events vulnerable to rejection though later processing. This tool, the result of work at Pennsylvania State University and the Massachusetts Institute of Technology, helps limit the subsequent non-uniform gain across, and the degradation in energy resolution towards the top of, the detector [92]. Events with energies greater than 10 keV were then removed with the `filter.csh` tool. Since N103B is an extended object, it is necessary to create a custom mask which defines the region shape, size, and orientation in sky pixel-plane coordinates for both the zeroth-order and two (HEG and MEG) diffracted orders. This was performed with `tg_create_mask.csh` and `tg_resolve_events.csh`, which allow wavelengths to

be deduced from the spatial locations of the diffracted events on the detector. Events recorded at times when the aspect solution of the satellite is poor were excluded with `lightcurve.csh`. Pixels flagged by the *CXC* were excluded, as were events culled by hand after minutely examining the data. Finally, `destreak.csh` was employed to eliminate the pattern of streaks that occur on the ACIS-S4 chip due to a faulty serial readout which randomly deposits charge along pixel rows. Flares did not affect the observations.

Spectra (`pha` files) and their corresponding `arf` and `rmf` files were created using custom MIT "filament analysis" software to take into account the extended size of N103B [18]. `ISIS` version 1.0.39 was used for all model fitting; atomic emission line information is provided by the Astrophysical Plasma Emission Database (APED), `neivers 2.0`, imported from `XSPEC V11.2`, which includes improvements as such radiative and dielectronic recombination (continua and lines), L-shell line emission, two-photon continuüm emission, selected inner-shell processes, and inclusion of Ar atomic data [9].

3.4 Zeroth-order and Dispersed Images

Zeroth-order images of the SNR were produced by using the moderate ACIS energy resolution, like those in Figures B-2 and B-4, and compared to precise images of particular emission lines formed by examining the HETG dispersed data at 12 to 13 Å, 14.5 to 18 Å, and 18 to 20 Å.

Images of emission attributable to [Ne X] and [O VIII] are presented in Figures B-3 and B-5. These are the first HETG images obtained from N103B of O and Ne, showing the spatial distribution of the elements in the remnant in greater detail than available from the moderate energy resolution of ACIS zeroth-order images. All images show the same east-west asymmetry seen in X-ray and radio maps, in which the western hemisphere is some three times brighter than the eastern side. However, important morphological differences exist. Whereas the oxygen emission peaks towards the northwest, neon (and magnesium) emission is more prevalent in the south and south-

west. Iron maps, reproduced in Figure B-6, show Fe rather evenly distributed, with some distinctive differences between the various Fe emission lines, reflecting variations in temperature and abundance across the remnant. Considering the X-ray emission images altogether, there is good evidence of substructure present, especially in the western hemisphere.

In order to determine the implications for the classification of the remnant, we searched for quantitative comparisons of the elemental abundances to those in supernova models.

3.5 The Global Spectrum and Astrophysical Plasma Models

A global spectrum was produced by collapsing the count data perpendicular to the dispersion axis for both the MEG and the HEG. Figure B-7 shows a global spectrum mosaic created from the four grating orders; atomic emission lines are broadened mainly because of observing an extended rather than point-like source; the line shapes are definitely not Gaussian, but rather approximate the overall brightness distribution of the remnant, whose flux is three times greater to the west. Many emission lines are clearly discernible from elements in ionized hydrogen- and helium-like states, including: S ($\lambda\lambda$ 4.72, 5.03, 5.06, and 5.10 Å), Si ($\lambda\lambda$ 5.21, 5.68, 6.18, 6.69, and 6.74 Å), Mg ($\lambda\lambda$ 7.47, 7.85, 8.41, 9.16, 9.23, and 9.31 Å), Ne ($\lambda\lambda$ 12.13, 13.52, 13.55, and 13.70 Å), Fe ($\lambda\lambda$ 14.21, 15.01, 15.26, 17.05, and 17.09 Å), and O ($\lambda\lambda$ 18.63, 18.97, 21.60, 21.80, and 22.10 Å).

Figure B-8, which displays the contribution of our derived iron contribution to the global spectrum, as predicted by shock modeling (*see* Section 3.5.2), demonstrates the complexity the iron emission adds to the spectrum, especially when the iron possibly exists at multiple temperatures. Great care is required to accurately deduce the relative elemental abundances in this remnant, as the iron emission contributes to a large swath of the overall spectrum detected; essentially, only Si, S and O emission are

left relatively unaffected by the Fe emission. This makes the Hydrogen-like [Si XIV] and Helium-like [Si XIII] emission lines, which also have the highest count statistics in the spectrum, ideal for two-dimensional spectral modeling, discussed below in Section 3.6. The relative elemental abundances are normalized to Si due to this reason and the fact that relative abundances are more consistent among SN models than absolute abundances [39].

In order to understand the N103B spectrum, model assumptions must be made to generate a model spectrum, which is then folded through the known instrument response to obtain a "detected" model spectrum equivalent to the spectrum actually detected and recorded, and to which the model spectrum may be compared. The luminosity distribution of the zeroth-order image was used to estimate the shape of the emission line in the model spectra. Three important models are common in studies of SNRs, each embodying unique assumptions of the physical processes present and evolutionary history of the remnant. One of these is the Collisional Ionization Equilibrium thermal emission model [74], or Mewe-Kaastra plasma model [41], which has as parameters merely a plasma temperature, the metal abundances, and a redshift. It is the simplest model to describe, but is completely unphysical as it ignores the fact that the ionization timescales are comparable to or exceed the age of the remnant. The Nonequilibrium Ionization emission model, with a constant temperature, and a single ionization time-scale, has as parameters temperature, heavy element abundances, the ionization age $\tau = n_e\ t\ (s\ cm^{-3})$, and the redshift [9]. The NEI model relaxes the equilibrium condition of the CIE model, but it is also simple, consisting of an impulsively heated, uniform and homogeneous gas with density n_e, initially cold and neutral. Though it allows for better characterization of spectra, it is still not a physical model. Heavily used in modeling SNRs, it is unlikely to be an accurate approximation to shock-heated plasmas. The plane-parallel shock plasma model [9], with separate ion and electron temperatures (in our case set equal), has, as additional parameters to those of the NEI model, upper and lower limits of the ionization time-scale. Plasma temperatures are defined as the average energy per particle (ions and electrons) and are constant throughout the postshock flow.

All of our modeling included photo-electric absorption, `wabs`, between the source and observer, modeled using $M(E) = e^{-N_H \sigma(E)}$, where N_H is the equivalent hydrogen column density, set to the *XMM-Newton* best-fit value of $2.5 \times 10^{25}\ m^{-2}$ [34], and $\sigma(E)$ is the photo-electric cross-sections using Wisconsin values [66]. All models also include a non-thermal component, `srcut`, described by a synchrotron spectrum from an exponentially cut-off power law distribution of electrons in a homogeneous magnetic field [76, 77]. Justified by the presence of non-thermal emission in the radio spectrum, it gives the maximally curved physically plausible spectrum; it has three parameters: a radio spectral index set by radio observations ($\alpha = 0.67$), a normalization, given by the 1 GHz flux (0.73 Jy), and a break frequency, which we set at the maximum frequency consistent with our spectra ($2 \times 10^{17}\ Hz$). This non-thermal component, however, only contributes a small fraction of the total emission.

3.5.1 Non-Equilibrium Ionization Modeling of N103B

Van der Heyden *et al.* [34] employ CIE and NEI models in the SRON `SPEX` package to fit their *XMM-Newton* data. In order to test if our *Chandra* spectrum agreed reasonably well with their spectrum, we employed the NEI model from the `XSPEC` library imported into `ISIS` to derive a 1-D simultaneous fit to our four orders of spectral data.

First, a one-temperature NEI model was tried; this approach failed to adequately explain the data.

We then attempted to fit the four spectra orders of the HETG with a three-temperature NEI model which adopted the best fit temperature (kT = 3.5, 0.65, & 0.55 keV) and $n_e t$ values published by van der Heyden *et al.* [34]. It fits the observed spectra well, with a reduced $\chi^2 = 1.247$. Their *XMM-Newton* best-fit column density of $25 \times 10^{20}\ cm^{-2}$ was assumed throughout all model fitting. The elemental abundance ratios implied by this model are given in Table A.1, and compared to those derived by van der Heyden *et al.*; relative uncertainties are largest for the oxygen ratio as the rapidly dropping effective area affects those wavelengths the most. The fair agreement between the two model results implies that the *XMM-Newton* and *Chandra* spectra are

reasonably similar, and that it is possible to compare the two, as well as the results of the different software analysis tools. As has been previously noted elsewhere and seen in Table A.1, the disagreement between the N103B and the mean LMC abundance values forcibly argues against an older, snowplow-stage hypothesis for N103B, and a swept-up ISM interpretation of the X-ray spectra [37, 34, 49].

3.5.2 Shock Modeling of N103B

Previous NEI modeling has indicated that some of the emission can be attributed to hot ($3.5\ keV$) emission with ionization ages as low as $n_e t = 5.3 \times 10^{10}\ scm^{-3}$, implying a very recent shock heating of 200 years [34]. Thus, it is natural to attempt shock models of the spectra; here we used the `VPSHOCK` model from `XSPEC` library imported into `ISIS`.

Even though no previous attempts have been made to use a shock model to fit their data, similar results from the NEI fits of *Chandra* and *XMM-Newton* spectra tend to argue that our shock model is both an independent test of their derived abundance ratios and probably similar to results they would have obtained if they had used such a model on their own data.

Single-temperature shock models do not adequately reproduce the global spectrum, and thus, fail to explain the data.

A two-temperature shock model was successful, however, in simultaneously fitting all of the four spectral orders of the *Chandra* HETG to obtain a reduced $\chi^2 = 1.11$. The ionization age and abundance of each element were free to vary to achieve a good fit, with the imposed assumption that there be an equal amount of each element at either of the two temperatures. The motivation for the two temperatures stem from an inability to model the entire range of the spectra with only one temperature free to vary; instead, the temperatures here were fixed at $0.66\ keV$ and $2.2\ keV$. The lower temperature was motivated by a single temperature fit of only the $14.6 - 17.4$ Å (Fe dominated) region, whereas the higher temperature was required by a single temperature fit of the $5.6 - 7.5$ Å (Si emission) region. Thus, while Fe-K in the *XMM-Newton* spectra necessitated a hot plasma at a temperature of several keV,

we find a similar need in a careful analysis of the [Si XIV] and [Si XIII] emission lines. The corresponding elemental abundance ratios implied by the model are given in Table A.2 and Figure B-9, and contrasted with Type Ia and II abundance predictions given by Iwamoto *et al.* [40] and Thielemann, Nomoto, and Hashimoto [89].

Figure B-11 is the a plot of shock model contours of constant emission line flux ratio in time/temperature space, for hydrogen-like and helium-like Si emission. The quoted best single temperature and ionization age model values of the Si region are marked by the cross. Simple Gaussian fits (with continuüm) of the spectrum imply a model independent ratio of [Si XIV] to [Si XIII] emission to be 0.239; a more complete two dimensional spectral analysis (discussed below, in Section 3.6) of the dispersed Si lines imply a flux ratio of 0.258, in agreement to within 10%. Thus, any shock fit along this constant ratio line of 0.239 will change the χ^2 value relatively little; one interpretation is that the constant ratio defines a lower limit on the temperature of 1.13 keV (1.1×10^7 K), and a lower limit on the ionization age, τ, of 1.1 kyr (3.5×10^{10} s cm^{-3}).

Similar results are obtained for the other line ratios in the $14.6 - 17.4$ Å (Fe dominated) region that was used to define the lower 0.66 keV temperature for the shock modeling. Figures B-12, B-13, B-14, and B-15 show the corresponding Fe line ratio plots for the four ratios considered. The ratios considered were: [Fe XVII] $\lambda\lambda$16.78, 17.05, and 17.09 Å flux to [Fe XVII] $\lambda\lambda$15.01 and 15.26 Å flux; the [Fe XVIII] λ16.073 Å flux to [Fe XVII] $\lambda\lambda$15.01 and 15.26 Å flux; the [Fe XVII] λ15.26 Å flux to [Fe XVII] $\lambda\lambda$15.01 and 15.26 Å flux. [Fe XVII] λ16.78 Å flux to [Fe XVII] $\lambda\lambda$16.78, 17.05, and 17.09 Å flux. Simple Gaussian fits (with continuüm) of the spectrum yield ratio values of 0.71, 0.63, 0.11, and 0.25, respectively. Considering the four Fe ratios together defines a lower limit on the temperature of 0.56 keV (1.1×10^7 K), and a lower limit on the ionization age, τ, of 0.6 kyr (2×10^{10} s cm^{-3}). This is evidence that the three-temperature model used by van der Heyden *et al.*, which include a 0.55 keV, a 0.65 keV component, and a hot, multiple keV component is encompassed by our two-temperature shock model. In this case, our 0.65 keV component at a range of τ's is equivalent to the two lower-temperature components of van der Heyden *et al.*

Among the remaining emission lines only those of oxygen escaped being overlapped by other elemental emission, so the [O VIII] to [O VII] ratio was treated similarly, with the Gaussian fits implying a flux ratio of 1.51; the overall lower limit on the temperature is thus 0.40 keV (3.9×10^6 K), and a lower limit on the ionization age, τ, of 25 kyr (8×10^{11} $s\ cm^{-3}$). We note that only a slight shift to the left in Figure B-16 would scarcely affect the temperature while dropping the lower limit on τ to 1.6 kyr.

The close agreement between the flux ratio measured by Gaussians and that predicted by the shock model, especially in the case of Si, which has the best count statistics and the least interference with other line emission, demonstrates that the model fits are at least self-consistent.

3.6 Spatial-spectral Analysis

Spectral-spatial analysis allows for studying the structure of the remnant across its surface. It should be possible to detect temperature and density fluctuations across the SNR due to changing spatial distributions of line fluxes, as well as Doppler shifts due to velocity structure, which affect the plus and minus dispersed orders of the HEG and MEG differently [18]. Due to count limitations, the application of the spectral-spatial software is limited to the Si emission.

Employing software tools developed at MIT by D. Dewey, we do not require, in preliminary analysis, either appreciable ($> 500\ m\ s^{-1}$) overall Doppler shifts, nor significant ($> 1000\ km\ s^{-1}$) velocity broadening to explain the differences in the width of the Si region in the plus and minus orders of the dispersed two-dimensional spectra.

Chapter 4

N103B Implications

TEKEL*; Thou art weighed in the balances, and art found wanting.*

- Daniel 5:27

Using models of emission from mean LMC abundances, and comparing them to those of the SNR, we find that the swept-up mass must only be a small fraction of the total emitting mass, implying that the remnant is in the ejecta-dominated phase. This argument is strengthened by indicators of the age of N103B, as seen from the small radius of remnant in radio, optical, and X-ray wavelengths, and as extrapolated from the fit parameters of the shock modeling.

Even with swept-up interstellar matter contamination thus being eliminated, the corresponding measured elemental abundance ratios do not clearly favor one type of progenitor over the other when compared to SN models. Essentially, the uncertainties in the observed abundance ratios are dominated by the many assumptions that enter into the modeling. While shock models are heavily relied upon as physically plausible, two-temperature shock models require implicit assumptions of the distribution of the elements at the various temperatures. Calculating the age of the remnant from shock model ionization ages also requires assumptions.

4.1 Age estimate of N103B

It has long been assumed on the basis of N103B's small (3 pc) radius that the remnant's age is $\leq$ 1500 yr; only one dissent from this conclusion has appeared [34]. Given the volume emission measure ($n_e n_H V$, where n is the species density and V is the volume filled by emitting matter) and the ionization age ($n_e t$, where t is time) the age of the remnant can be written as

$$t \simeq n_e t \sqrt{\frac{V}{n_e n_H V}}. \tag{4.1}$$

While van der Heyden *et al.* acknowledge that Equation 4.1 is evaluated using only an estimate of the volume, it is still worthwhile to examine their argument, which reproduces the commonly accepted age to within a factor of two. Using their numbers of $n_e t \geq 250 \times 10^{16}\ s\ \ m^3$, $\ n_e n_H V = 65.2 \times 10^{64}\ m^{-3}$, and $V = V_{shell} \times f_{macro}$, where shell's volume, V_{shell}, is $1.78 \times 10^{51}\ m^3$ and the macro-fill factor, f_{macro}, is 0.5, motivated by the high luminosity of the western hemisphere, the age is indeed $\geq$ 2900 yr.

However, the inclusion of a micro-fill factor has been neglected. Many SNRs have shown strong evidence of clumping and small-scale structure, and N103B is no exception, having both bright knots and filaments [48]. A micro-fill factor is warranted, and a $f_{micro} = 1/5$ is easily plausible. Such a fill factor would bring this estimate into agreement with standard N103B age estimates of around 1300 yr.

4.2 Re-classification of N103B

In order to limit the degrees of freedom in the modeling process, the multi-temperature shock models commonly have the abundances at the various temperatures arbitrarily fixed together in some ratio: in our case, we fixed the amount of all elements, except Fe, as equal at the two temperatures. In the case of the lighter elements, this may lead to an overestimate of the amount of each element present. For example, the O emission is dominated by the lower temperature component; the model, however,

will require an equal amount of O at the higher temperature, even though such fully ionized O will not emit and therefore, not contribute to the observed spectrum.

Thus, the two-temperature shock model abundances, given in Figure B-9 may be interpreted as an upper limit of the amount of each element present. To determine the lower limit, we extrapolate the abundances by only including the minimal amount of each single ion species at a median temperature of 0.8 keV. These abundances are shown in Figure B-10. Interpreted in this manner, the true elemental abundances fall somewhere between the N103B model abundances plotted in Figures B-9 and B-10. For elements heavier than Si, there is not much difference between core-collapse and Type Ia abundances, until one considers large ($\geq$ 20 $M_{\odot}$) progenitors.

Our shock model abundances are equidistant from Type Ia and II predictions for element heavier than Si. The limits of the lighter elements fall neatly between the Type Ia and II predictions, precluding a definite progenitor classification one way or another. However, we note that the conditions imposed to form the lower limit are extreme: the smallest possible abundance of each element is responsible for the emission, by virtue of the fact that each element is at a temperature that is optimum for maximum emission. As there is good evidence for multiple temperature plasmas in N103B, and since it is unlikely that the elements would be segregated optimally at the different temperatures at which they would be most efficient emitters, then the upper limit, *i.e.*, the two-temperature shock model abundances shown in Figure B-9, are our best indication of the true quantity of each element. Ne and Mg are particularly close to the prediction for 13 $M_{\odot}$ core-collapse SNe; the heavier elements also agree more closely with a smaller 13 $M_{\odot}$ rather than larger 20 $M_{\odot}$ Type II supernovae.

Thus, we consider it most plausible, given our data, that N103B is the aftermath of a core-collapse supernova in a $\sim$ 13 $M_{\odot}$ star, but cannot rule out categorically a Type Ia origin. Our Type II conclusion would resurrect the possible and previously assumed association of N103B with large star cluster NGC 1850.

Chapter 5

The Puzzle: CTB 80 and the Radio Pulsar B1951+32

> *Light though thou be, thou leapest out of darkness ... There lies my puzzle; but thine is greater. Thou knowest not how came ye, hence callest thyself unbegotten; certainly knowest not thy beginning, hence callest thyself unbegun. I know that of me, which thou knowest not of thyself, oh, thou omnipotent. There is some unsuffusing thing beyond thee, thou clear spirit, to whom all thy eternity is but time, all thy creativeness mechanical. Through thee, thy flaming self, my scorched eyes do dimly see it.*
>
> - Herman Melville, **Moby Dick**

Associations between pulsars and supernova remnants allow measurements which would not be possible on either population of object alone. Since the center of an SNR marks the presumed pulsar birth-site, the pulsar's characteristic age, combined with the offset of the pulsar from the center of the SNR, lets us estimate the pulsar's transverse velocity [27]. A more difficult feat is to actually measure such a pulsar's proper motion.

Determinations of the proper motions of neutron stars are crucial for several important reasons. First, the direction of motion can confirm (or refute) associations with individual SNRs. Secondly, such motions are needed in observationally establishing that neutron stars are formed in the center of supernovae. Finally, the magnitudes

of the motion, coupled with determinations of the angular offset from the birth-site of neutron stars, gives an independent estimate of pulsars' ages, independent of the neutron stars' distance from us (Earth) [29].

Ages of neutron stars can in turn be used to test models of neutron star cooling and otherwise place constraints on the nature of high density matter. Ages of pulsars can be used to establish their initial pulse periods, distributions of which could be employed to test theories of pulsar formation and formation mechanisms. Lastly, neutron star ages help establish the number and birth rate of such stars in the Galaxy, which then can be compared to the Galactic supernova rate, in order to determine the fraction and types of supernovae that form neutron stars, a rather basic quantity that is unknown at the present time.

5.1 The Supernova Remnant CTB 80

CTB 80 (G69.0+2.7, W 56, also known as the "Rabbit") is an extended, strongly polarized, non-thermal Galactic radio source, properties which led it to be first considered as a supernova remnant in 1970 [21], and later confirmed as such after 11 *cm* observations in 1971 by the 300-ft. telescope at Green Bank [95].

It was immediately recognized as a more complex source than most SNRs; morphological studies of CTB 80 in the radio band revealed it as a composite type remnant consisting of a plerionic (*i.e.*, center-filled) component at the south-west edge of a larger component, which is nearly circular in the north, and shell-like over the greater part except around the aforementioned plerion [95, 96, 3, 87, 54]

This compact nebula (plerion) consists of $30'$ long radio emission ridges, which intersect a $10'$ by $6'$ plateau region with a fairly uniform spectral index $\alpha = 0.4$, containing an extremely flat ($\alpha = 0$ spectrum between 49 and 2.8 *cm*) compact source of $30''$ diameter at the south-western part of the plerion near the brightest rim of radio emission. The radio emission is linearly polarized to a high degree (between 15% and 30%) over large areas of the compact and extended regions suggesting a Crab-like remnant [99].

Spectral studies of optical nebulosity associated with the plerion reveal low velocity gas whose spectral line ratios are consistent with collisional excitation, and the velocity field suggests the broken shell is expanding at 35 $km\ s^{-1}$, all of which strengthens the SNR hypothesis [2].

At higher resolution, the plerion shows evidence for limb-brightening [87]. [H I] absorption suggests a distance to the SNR of 2.4 ± 0.2 kpc [88].

5.2 PSR B1951+32

In 1988, very fast radio pulsations with a period of 39.5 ms were detected from the point source in the plateau region of the plerion component of CTB 80 [46]. This pulsar, PSR B1951+32, is spinning only slightly slower than that of the Crab Nebula; however, its low period derivative, about 100 times smaller than for the archetypal pulsar of the Crab, indicates a much larger characteristic age, $\tau_c \equiv P/2\dot{P} = 107\ kyr$, and a much lower surface magnetic field, $B \approx 5 \times 10^{11}\ G$ [28].

Optical observations reveal a ring of amorphous red nebulosity of angular diameter $\sim 50''$ containing knots coincident with the central radio source. The pulsar is inside the central $1'$ core that emits strong [S II], [N II], and [O I] relative to Hα [2, 8, 33, 101].

A $\sim 1^\circ$ diameter shell of infrared emission, shown in Figure B-17, is centered $\sim 30'$ eastward of the pulsar and coincident with the [H I] shell, both of which are almost circular excepting the open south-western portions [45].

The first X-ray observations, made with the *Einstein* satellite, showed a centrally located point source coincident with that in the radio and surrounded by a diffuse emission of $\sim 1'$ radius harboring the pulsar and compact radio nebula (plerion) [6]. More diffuse emission from an X-ray nebula extends $\sim 5'$ eastward of the pulsar's position. X-ray pulsations were detected in 1995, with an implied pulse fraction of 35% [82]; the X-ray emission from the compact core and extended diffuse nebula can be explained satisfactorily as synchrotron radiation from the relativistic pulsar wind confined by the ram pressure of the surrounding inhomogeneous medium [98, 68, 1]. Pulsations from B1951+32 have been also detected in γ-rays [73].

The estimated dynamic age of 7.7×10^4 $d_{2\ kiloparsec}$ years agrees well with the spin-down age. This fact, B1951+32's location at the peak of the radio emission, and the similarity of the pulsar's distance (2.4 ± 0.2 *kpc* as estimated by its dispersion measure) to the SNR's distance (2 *kpc* as measured with [H I] absorption [88]), strongly suggest that the SNR shell is physically associated with the birth of the pulsar. This system, however, appears quite different from more typical pulsar/SNR associations, in which a young ($\tau_c \leq 20$ *kyr*) pulsar sits near the center of an approximately circular shell.

5.3 Theories of Evolution

The difference between the CTB 80 system and other, more typical pulsar/SNR associations can be understood if one invokes an evolutionary scenario proposed by Hester and Kukarni, in which the pulsar, core, plateau, and extended components of CTB 80 are all related to a single (Type II, *i.e.*, core-collapse) supernova event [22, 33, 45].

Specifically, this models posits the following sequence:

• The pulsar and the SNR are formed in the same supernova explosion, presumably either by the pulsar being formed in the core of the supernova or by the pulsar being created out of a nearby star in a binary system in which the supernova progenitor existed (Figure B-18, top). As the size of the wind bubble produced by the progenitor star must have been smaller than the current size of the SNR shell, the supernova probably originates in a star of main-sequence spectral type B0 or later.

• The pulsar is given a kick by asymmetries in the supernova explosion, giving it an approximately south-westward velocity. As the SNR originally expands at a much higher velocity than at the present time, at early times the system indeed consists of a pulsar sitting within its associated SNR.

• The SNR evolves rapidly in the interior of the low-density cavity surrounding the progenitor. During this time, the blast wave remains adiabatic and interior pressure high, and the blast encounters a nearby cloud of denser material, resulting in a temporary brightening as momentum of the blast is converted into pressure. Else-

where, the remnant gradually decelerates but continues to expand as it sweeps up surrounding material. As overpressure abates, the SNR fades from view, especially at X-ray energies, except in the south-west region where it encounters dense ambient material (Figure B-18, center).

• After 10^5 years, the pulsar eventually catches up with and begins to penetrate the SNR shell, which is mostly inconspicuous at radio and X-ray wavelengths and distorted by the size and shape of the preexisting dense cloud. The large solid angle subtended by the cloud makes it not unlikely that the pulsar should penetrate the portion of the shell that interacts with the cloud. The pulsar's relativistic wind, carrying away its spin-down energy, then interacts with the SNR shell, in which the wind is confined, re-energizing it and further distorting it by driving the shocks responsible for the bubble-like optical core (Figure B-18, bottom). The X-ray emission is explained by synchrotron radiation from the particles carried along in the wind. The bright arc seen immediately to the south-west of the pulsar in Figure B-20 (right) can then be interpreted as a bow-shock, produced by the balance between the pressures of the relativistic pulsar wind and of the gas in the SNR [84].

This sequence can explain both the strange appearance of CTB 80 and the large age of B1951+32 compared to younger, more typical pulsar/SNR associations. Furthermore, it places this system into an evolutionary sequence beginning with younger systems, like the Crab and Vela SNRs, then carrying through to older systems in which the pulsar is significantly offset from the center of its associated SNR (*e.g.*, PSR B1853+01 in SNR W 44 [27]), and extending to cases where the pulsar has apparently completely pierced its SNR and is now interacting with the ambient Interstellar Medium (*e.g.*, "the Duck," PSR B1757-24 in SNR G5.4-1.2 [42]).

However, other models have been suggested to explain the double enigma of the peculiar morphology of CTB 80 and its large age. One such alternate proposal, which addresses the morphology, hypothesizes that CTB 80 is actually the result of three supernovae [54]. Despite the evidence for an age comparable to the pulsar's characteristic age of $\sim 10^5\ yr$, several have put forth that the age may really be less than $10^3\ yr$, based upon the compact core and associated X-ray emission [86, 98].

Another proposition interprets the whole plateau and compact core region as a pulsar-illuminated progenitor wind-zone; the center of the proposed wind-zone is much closer to the pulsar than the Hester and Kulkarni prediction, requiring a much smaller proper motion given the large age of 10^5 years [47], a prediction which clearly can be tested by observations.

So, while the Hester & Kulkarni four-point evolutionary picture is æsthetically pleasing, it is imperative that it be verified by observations. Specifically, this proposed model of CTB 80 can be tested by measuring the proper motion of PSR B1951+32. If the two sources are associated, then the pulsar should be moving away from the center of the SNR, as defined by the shell seen in infra-red and [H I] [22, 45], as envisaged by Hester & Kulkarni. The separation between the pulsar and the shell's center, when combined with the pulsar's characteristic age, lets us predict a proper motion for the pulsar of $\mu \approx 15\ mas\ yr^{-1}$ at a position angle (PA) $\approx 250^\circ$ (north through east), independent of the distance to the system. A proper motion of that magnitude, regardless of position angle, would rule out an illuminated wind-zone hypothesis.

Chapter 6

PSR B1951+32 Observations and Analysis

What seest thou else
In the dark backward and abysm of time?

- William Shakespeare, **The Tempest**

PSR B1951+32 shows significant timing noise, which prevents measurement of its proper motion through time-of-arrival analysis [25, 26]. Thus, only via interferometric measurements can this prediction be tested.

6.1 Very Large Array Observations

The Very Large Array (VLA) is a radio interferometer consisting of twenty-seven radio antennas, each measuring 25 m in diameter, in a Y-shaped configuration. Located on the Plains of San Agustin, some 50 miles west of Socorro, New Mexico, the VLA detected its first fringes in 1976. The array can be deployed in four configurations, with a maximum antenna separation of 36 km (A array), to a minimum separation of 1 km (D array). The frequency coverage extends from 74 to $50,000$ MHz (400 to 0.7 cm); the highest frequency and greatest antenna separation sets the resolution limit of 40 milliarcseconds. The minimum elevation angle is 8° above the horizon,

and the antennae have slew rates of 40° and 20° per minute in azimuth and elevation, respectively.

Additionally, the 2000-epoch observations were able to draw advantage from the new Pie Town link, a real-time, fiber optic connection with the Pie Town antenna of the Very Long Baseline Array (VLBA) that entered into service that same year. Doubling the longest baseline of the VLA, the Pie Town link thereby doubles the resolution of the VLA.

Observations of PSR B1951+32 were made with the VLA at epochs 1989.04, 1991.55, 1993.02 and 2000.90. The first three observations were archived and part of a campaign conducted by Foster & Backer to measure B1951+32's proper motion (projects AS 357, AF 214, & AF 235) [25], while the last observation was proposed by Gaensler, Backer, *et al.* (project AG 602) [63]. Each observation was eight hours in duration and used the VLA's A configuration, with a minimum baseline of 680 m, and a maximum baseline of 36 km providing a maximum resolution of $1\farcs1$ for signal wavelengths of 20 cm (L Band). The data recorded were cross correlated (RR polarization). In the 1989-, 1991-, and 1993-epoch observations, data were recorded at two simultaneous frequencies, 1385 and 1652 MHz, within the 20-cm band, which coincides with the pulsar's peak flux density, for an optimal signal-to-noise ratio. The pulsar's continuous flux density of 1 mJy at 20 cm can, however, vary significantly, which requires the eight-hour observations to be divided into smaller intervals to mitigate this potential error in the deconvolution process. Each frequency consisted of 15 channels spread across a 23.5 MHz bandwidth ($\delta\nu = 1.56\ MHz$) with a sampling time of 10 seconds, resulting in a usable field-of-view of $\sim 10'$ radius centered on the pulsar. Smearing problems precluded the employment of relative astrometry in similar, single-channel 20 cm VLA observations of PSR B1951+32 taken in 1987, 1985, and earlier years, which could have significantly extended the eleven year baseline but were limited by the unpartitioned 25 MHz bandwidth to a usable field-of-view of less than $2'$, which lacked extragalatic reference sources. In the 2000-epoch observations, which incorporated data from the Pie Town antenna of the VLBA, the resulting increased resolution was attained in primarily one dimension only, owning to the limited

u-v coverage realized in an eight hour period. The observations were conducted at 1385 and 1516 MHz, and consisted of 15 channels across a 12.5 MHz bandwidth with 5-second sampling, again resulting in a 10-arcminute field-of-view. The flux density scale of our observations was determined using observations of 3C 286, while the time-varying gains for each antenna were measured using regular observations of PKS B1923+210 or TXS 2013+370.

6.2 Data Reduction

The data were converted to `FITS` format; the data reduction was performed exclusively in the "Multichannel Image Reconstruction, Image Analysis and Display," or `MIRIAD`, standard software package [83]. `MIRIAD` is a radio interferometry data reduction and analysis tool originally written in `Fortran 77` as developed in 1987 by the Berkeley-Illinois-Maryland Array (BIMA) project; it is commonly used for analysis of data from the Australia Telescope Compact Array.

We first flagged incongruous data points, accomplished with the `MIRIAD` tools `QVACK, BLFLAG,` and `UVFLAG`. Additionally, channel fifteen was removed from all data sets, as it was found to have been significantly degraded as a result of decreased sensitivity attributable to roll-off at the edge of the bandpass filter. The primary calibrator for the data, providing the bandpass correction as a function of time, was 3C 286 (1331+305). The corrections were then copied to the secondary calibrators, PKS J1925+2106 for 1989, 1991, and 1993, and TXS 2013+370 for 2000, from which the gains and phases were extrapolated. Finally, the gain tables, flux scales, and bandpass solutions were all copied to the pulsar field. The `MIRIAD` tools used in these manipulations were thus `MFCAL, GPCOPY,` and `GPBOOT`.

After the data were flagged and calibrated, reference source candidates were identified in a wide-field image, and then 512×512 pixel images were created with `INVERT` centered on each source, with a pixel size of $0\farcs1$ ($0\farcs05$ for year 2000 data), to render ~ 10 pixels beam^{-1}.

We next produced images of the pulsar field for each epoch and frequency, us-

ing multi-frequency synthesis to mitigate bandwidth smearing, a robust weighting of zero, and discarding all baselines shorter than 10 km (corresponding to spatial scales larger than $4''$). By removing these shorter baselines, we ensured that emission from SNR CTB 80 and from the compact wind-driven nebula surrounding the pulsar were not detected. The only emission seen in our images was the pulsar itself, the "hot-spot" or bow-shock located immediately adjacent [86], and various other point sources spread throughout the field. However, a 20% reduction in the signal-to-noise ratio did result from this exclusion of longer baselines. We have identified ten such point sources within an angular radius of $15\farcm5$ of the pulsar, but we were limited to the seven sources that were not affected by bandwidth smearing, *i.e.*, that lay within the usable field-of-view of radius $10'$ centered on the pulsar. These seven sources are listed in Table A.3. After de-convolving the images to remove sidelobes with `MIRIAD` tools `CLEAN` and `RESTOR`, we applied a Gaussian fit using `IMFIT` to the pulsar and to each of the seven sources to measure their position and extent at each epoch and frequency.

In order to accurately measure the pulsar proper motion at a resolution of milliarcseconds per year, we employed relative astrometry, adopting six of the field sources as reference sources, and reserving the nearest source to the pulsar (Source 1 in Table A.3) as a check on our measurements. The reference sources are approximately evenly distributed throughout the field. The quality of each source as an astrometric reference was determined by measuring the vector separation between all possible pairs of sources, and then verifying that no source showed trends or significant changes in the magnitude and direction of these vectors. We also verified that in all cases, the dimensions of the Gaussian fitted to the seven reference point sources and pulsar matched those of the synthesized beam, confirming that scatter broadening and bandwidth smearing (in the case of background sources) or scintillation (in the case of the pulsar) were not affecting our positional determinations.

The ionosphere can potentially distort the measured positions, producing a frequency-dependent angular displacement $\Delta\theta = k\,\theta\,\lambda^2$, where θ is the angular separation between a source and the field center, λ is the observing wavelength, and k is a constant.

By measuring θ for each source and each frequency, we found that k had a value consistent with zero, demonstrating that any ionospheric effects were dominated by other uncertainties in our measurements.

6.3 The Proper Motion of the Pulsar

McGary *et al.* [62] used the VLA to measure pulsar proper motions an order of magnitude smaller than that expected for PSR B1951+32 and found a variety of other ways in which the positions of reference sources can be distorted, including relativistic effects due to the Earth's motion, errors introduced by the VLA correlator, and additional empirical corrections which had no simple explanation. At the lower precision required here, we have accounted for all these effects simply by measuring the scatter in the position of each reference source between epochs.

We began by determining the vector distances between all possible pairings of the six reference sources. The standard deviations of the components of each vector in Right Ascension and Declination were computed for the four epochs; these were taken as the uncertainty for a particular pairing. This uncertainty was then decomposed between the two sources in that pair, the relative contributions of the two sources to the joint error being weighted inversely by each source's signal-to-noise ratio. We were thus able to derive an uncertainty in the position of each source for each pairing; these uncertainties were averaged over the five possible pairings to determine the best measurement of the true uncertainty in each coordinate for each source. This analysis was performed separately for observations at 1385 MHz and at 1516/1652 MHz. A mean reference position for each epoch and frequency was then determined by averaging together the positions of the six reference sources, weighting the contribution from each source inversely by its distance from the field center.

The separation between the pulsar's position and this mean reference position was then measured for each epoch and frequency, combining in quadrature the calculated uncertainties in the pulsar position with those determined for the reference position. The results of these measurements are plotted in Figure B-19, and show a clear motion

of the pulsar to the south-west. The flux density of the pulsar was higher during the 1993 observations than at other epochs, resulting in smaller uncertainties in the pulsar position for this measurement. The position of the pulsar listed in Table A.3 is consistent with previous determinations [26], but with larger errors due to the systematic errors discussed above. Such uncertainties in the absolute astrometry do not affect our proper motion measurement, which has been determined based on astrometry relative to nearby background sources.

As an independent test of our approach, we have similarly measured the proper motion for Source 1. As is shown in Figure B-19, no change in position is seen for this source, demonstrating that the motion measured for the pulsar is real and that the uncertainties have been realistically assessed.

By applying a weighted least squares fit to the pulsar's position at each epoch, we find a proper motion at 1385 MHz of $\mu = 31 \pm 5$ $mas\ yr^{-1}$ at PA $= 250^\circ \pm 7^\circ$, and at 1516/1652 MHz of $\mu = 26 \pm 6$ $mas\ yr^{-1}$ at PA $= 240^\circ \pm 10^\circ$. These two measurements are consistent with each other within their uncertainties. After taking into account apparent motion of the pulsar at the level of 5 $mas\ yr^{-1}$ due to differential Galactic rotation,[1] the combination of our two measurements yields a motion $\mu = 25 \pm 4$ $mas\ yr^{-1}$ at PA $= 252^\circ \pm 7^\circ$. The corresponding projected velocity is $V_t = (240 \pm 40)\, d_2$ $km\ s^{-1}$ for a distance $2\, d_2$ kpc.

[1]To make this calculation, we use the rotation curve of Fich, Blitz & Stark [23] and assume a 10% uncertainty in the systemic velocity of the pulsar.

Chapter 7

CTB 80 and B1951+32 Implications

Deep into the darkness peering,
long I stood there, wondering, fearing,
doubting, dreaming dreams no mortal ever dreamed before.

- Edgar Allan Poe, **The Raven**

The transverse velocity we have inferred for PSR B1951+32 is in agreement with the value $V_t \sim 300\ km\ s^{-1}$ implied by scintillation in its dynamic spectrum [28]. Furthermore, as shown in Figure B-20, the measured position angle of the proper motion agrees closely with the direction predicted if the adjacent "hot-spot" is interpreted as a bow-shock driven ahead of the pulsar [86]. It can also be seen in Figure B-20 that the pulsar is clearly traveling directly away from the center of its SNR. While this result is not unexpected given the already strong evidence for an association between the pulsar and SNR, it is surprising to realize that this is the first time such an effect has actually been observed. Such measurements for other young pulsars in SNRs have failed to demonstrate such motion, and have either required specific models of SNR and pulsar evolution to maintain the association [5, 29], or have caused the association to be abandoned [90].

While the direction in which the pulsar is moving is as predicted, the magnitude of

the pulsar's motion is not in agreement with the simplest expectations. By projecting the pulsar's position back by its 107 *kyr* characteristic age, τ_c, it can be seen from Figure B-20 (left) that its inferred birth-site is more than three standard deviations away from the geometrical center of its associated SNR. If the pulsar was born near the center of its SNR, then the pulsar's true age, t_p, must be less than τ_c.

7.1 Age Determination of the Pulsar and Supernova Remnant

We can make an initial estimate of t_p by simply identifying the offset, Θ, of the pulsar from the SNR's center. We estimate from the morphology of the infra-red shell shown in Figure B-20 that $\Theta \sim 27'$, so that $t_p = \Theta/\mu \sim 64\ kyr$. However, a high velocity progenitor and/or asymmetric SNR expansion can produce a significant offset between the pulsar birth-site and the geometric center of the SNR [78, 20, 35]. Given the complicated evolutionary history of CTB 80, it is perhaps overly optimistic to define a precise geometrical center and simply assume the pulsar was born there.

If the birth-site is not at the SNR's geometric center, there is no reason to expect the pulsar to be traveling away from that position [32]. However, the farther the birth-site from the center of the SNR, the less likely the pulsar should be moving in this direction by chance. We can therefore quantify the uncertainty in the pulsar's birthplace as follows. We assume that for a given angular separation ϕ from the SNR's geometric center, it is equally likely that the pulsar was born at any position on a circle concentric with the SNR and of radius ϕ. Thus, for a particular value of ϕ, we can compute the fraction of possible birth-sites which are consistent with the pulsar's direction of proper motion, PA $= 252^\circ \pm 7^\circ$. By considering the full range of values $0 \leq \phi \leq \Theta$, we can build up a probability distribution of possible pulsar ages, from the integral of which we can determine the 1σ confidence limits on ϕ. Using this approach, we find that the pulsar was born within $\pm 8'$ of the SNR's center, and that the age implied by our proper motion measurement is $t_p = 64 \pm 18\ kyr$.

These estimates are independent of the distance to the system and of the site of the supernova explosion; they depend only on the assumptions that an approximate geometric center can be defined for the SNR and that the pulsar is moving away from its birthplace. The age we derive is consistent with the estimate of 77 kyr, deduced from the expansion velocity of the [H I] shell coincident with the SNR [45].

7.2 Pulsar Characteristic Ages

It is not surprising that the CTB 80 system's true age is less than the pulsar's characteristic age.

The frequency derivative, $\dot{\Omega}$, is found to be negative for all pulsars; this observed regular increase in period has been generally accepted as attributable to the loss of rotational energy and angular momentum via ejected particles and electromagnetic radiation at the rotation frequency of the star. In most theoretical models, the retarding torque is proportional to some power, n, of the rotation frequency [53], *i.e.*,

$$\dot{\Omega} = -K\,\Omega^n\ , \tag{7.1}$$

where K is a positive constant, and Ω is the frequency of rotation. Consequently, n is known as the braking index, and according to Equation 7.1, it can be determined empirically by the additional measurement of the frequency's second derivative, $\ddot{\Omega}$:

$$n = \frac{\Omega\,\ddot{\Omega}}{\dot{\Omega}^n}\ . \tag{7.2}$$

Equation 7.1 is equivalent to

$$\dot{P} = (2\pi)^{n-1}\,K\,P^{\,2-n}\ , \tag{7.3}$$

where P and $\dot{P}$ are the pulsation period and its first derivative, respectively.

A theoretical calculation of the braking index by magnetic multipole radiation or by particle acceleration in the pulsar's magnetosphere requires knowledge of the field

structure, which might have significant higher-order multipole structure within a few stellar radii of the surface, and which should generally be variable over time. The time constant for field decay is given by [14]

$$\tau_D = \frac{4\sigma\, R^2}{\pi(z+1)\, c^2}\ , \tag{7.4}$$

where σ is the conductivity, R is the stellar radius, c is the speed of light in vacuum, and z is an integer corresponding to the order of the mulitpole field. For the lowest order (dipole, $z = 0$), τ_D seemingly corresponds to a time scale of 10^6 to 10^7 years, much greater than the pulsar ages contemplated herein. Accordingly, the overall structure of the magnetosphere beyond a few radii can be considered constant in time and is generally assumed to be dipolar.

Thus, a theoretical consideration of the neutron star's magnetic dipole radiation of energy results in a radiation reaction torque transmitted to the star by the magnetic field, given by [70, 71, 69]

$$N = \frac{-2\,(m\sin\alpha)^2}{3\,c^3}\ \Omega^3\ , \tag{7.5}$$

where m is the magnetic dipole moment and α is the angle between the magnetic and rotation axes.

In the case of energy loss by particle acceleration, various assumptions yield braking indices between 1 and 3 (*see* [53] for discussion). The first theoretical model to consider this form of energy loss in an approximately dipolar magnetic field results in a torque of the form [30]

$$N = \frac{-k}{8\,c^3}\ (B_0 R^3)^2\ \Omega^3\ , \tag{7.6}$$

where k is a constant of order unity depending on the details of the field structure. In both cases, $N \propto \Omega^3$, implying a braking index $n = 3$ by Equation 7.1.

Providing $n \neq 1$, integrating Equation 7.1 yields

$$t_p = -\frac{\Omega}{(n-1)\,\dot{\Omega}}\left[1 - \left(\frac{\Omega}{\Omega_0}\right)^{n-1}\right]\ , \tag{7.7}$$

where Ω_0 is the rotation frequency at time $t = 0$. Hence, if P is the rotation period today (and for constant moment of inertia, which is implicitly assumed, although perhaps a poor approximation for millisecond pulsars), the pulsar's true age is

$$t_p = \frac{2\tau_c}{n-1}\left[1 - \left(\frac{P_0}{P}\right)^{n-1}\right] , \tag{7.8}$$

where P_0 is its initial spin-period and the characteristic age is defined as before, $\tau_c \equiv P/2\dot{P}$. For $n = 3$ (pure magnetic dipole braking) and $P_0 \ll P$, Equation 7.8 reduces to $t_p = \tau_c$, but in general, neither such condition will be satisfied. While n has not been measured for PSR B1951+32, we find $1.5 \leq n \leq 3$ for the five pulsars which have had their braking indices measured (*see* Table A.4).

For $n = 3$, the range in t_p determined above implies $P_0 = 25 \pm 5\ ms$ for PSR B1951+32, while for $n = 1.5$ we find $P_0 = 29 \pm 3\ ms$. Combining these estimates, we find the initial period most likely falls in the range $P_0 = 27 \pm 6\ ms$. Again, this estimate does not depend on the assumed distance to the source.

Chapter 8

Conclusion

As remarked in Chapter 1, one ideally observes physical processes as they occur in order to understand them, whether it be oscillations of pendula, solar flares, or particle decay. The rare and unpredictable manifestations of supernovae makes this option rather difficult, and the results of such a patient approach uncertain. That it is possible to understand so much by inspection of SN debris is remarkable, that Nature provides mankind with luminous, visible remnants is fortuitous. Only by virtue of this fact can we know anything about the answer to a rather basic question first posed by mankind millennia ago: Do stars die?

Not only can we answer this question, we can, amazingly, pose and answer more difficult ones, such as, how do they die, and even, looking at the remains of dead stars in this and other galaxies: what were they and how did they live before they died? The means to answer such questions lies in a statistical approach, a slow process of constructing catalogues of remnants, pulsars, and their properties. Accordingly, future answers to these questions will result from improved samples of interesting properties, for comparison with theories and constraining unknown parameters, and improved instruments available for the measurement of such properties.

8.1 Pulsar Initial Periods and Proper Motion Detection

As listed in Table A.5, PSR B1951+32 joins a rapidly growing list of pulsars whose initial periods have been determined from their associations with either SNRs or historical supernovae. While these measurements span a reasonable range of initial periods, the data provide good evidence that radio pulsars are born as rapid rotators, with no evidence for a population of longer initial periods as has been sometimes proposed [97, 15]. On the other hand, it is becoming abundantly clear that the characteristic age can be an unreliable estimator of a young pulsar's age, with corresponding implications for associations with SNRs, pulsar velocities, and models for neutron star cooling. With many new pulsar/SNR associations now being identified at both radio and X-ray wavelengths, a statistically useful sample of pulsar initial spin periods, critically necessary in order to test neutron star predictions and constrain parameters, should soon emerge.

The improvement in instrumentation that allows such small proper motions to be characterized is attributable to VLA upgrades, especially electronic upgrades allowing subchannels across the observation bandwidth to decrease bandwidth smearing, and the new Expanded Very Large Array project, of which the Pie Town link was an early phase, that will increase resolution to as much as 0.004 arcseconds. Some observers have succeeded in measuring much smaller pulsar proper motions [62], due to improved techniques, such as "gating" to improve the signal-to-noise ratio, and due to an improved understanding of systematic effects, such as Lorentz contraction due to the Earth's motion, important progress surely will continue to be made in this direction.

8.2 The Supernova Remnant Population of the Large Magellanic Cloud

The reclassification of SNR N103B as Type II, which is indicated here but yet to be definitively made, would significantly change the known population of young SNRs in the LMC. Table A.6 lists the six remnants with X-ray diameters less than 10 pc [58], and thus with ages less than 1500 yr. A Type Ia classification for N103B would indicate a ratio of Type Ia to Type II + Ib of 1:1; revision indicates the ratio to be 1:2. This has large implications for testing predictions of SN rates, particularly in galaxies of Hubble type Sdm-Im. Van den Bergh & Tamman [7] suggest a ratio of 1:5, but judging from the small sample size, it may be premature to conclude for or against any particular model. However, the result would lower what had been an anomalously high absolute rate of Type Ia SNe in the LMC, compared to other late-type galaxies. Further studies may help determine if N132D, despite its large radius, may perhaps have an age comparable to 1500 yr and, therefore, belong in the young remnant population. Eventually, an improved understanding of supernovae and their progenitors will allow older remnants to be studied as well, which, when combined with those of the Small Magellanic Cloud, should provide an enlarged population for study and greater statistical certainty in the determination of SN rates.

Clearly, the *Chandra* High Energy Transmission Grating Spectrometer is a revolutionary instrument. For remnants with a small angular size, a small iron abundance, and thus well defined lines, like E0102 [24], the HETGS allows for unprecedented information on the X-ray structure of the remnant, as well as its composition and elemental distribution. Perhaps the most important tool needed for full use of the HETGS data is continued improvement of the spatial-spectral software in development [18], and especially the atomic data on which the fitting is predicated. Iron rich remnants, like N103B, are rather difficult to analyze, as constraining the many parameters of today's more physical models becomes subtle. It is hoped that future improvements will soon allow more definitive temperature, density, line broadening, velocity, and elemental abundance maps of remnants to be made.

Appendix A

Tables

Si je vous ai raconté ces détails sur l'astéroïde B 612 et si je vous ai confié son numéro, c'est à cause des grandes personnes. Les grandes personnes aiment les chiffres. Quand vous leur parlez d'un nouvel ami, elles ne vous disent jamais: "Quel est le son de sa voix? Quels sont les jeux qu'il préfèr? Est-ce qu'il collectionne les papillons?" Elles vous demandent: "Quel âge a-t-il? Combien a-t-il de frères? Combien pèse-t-il? Combien gagne son père?" Alors seulement elles croient le connaître... Mais, bien sûr, nous qui comprenons la vie, nous nous moquons bien des numéros!

- *Antoine de Saint-Exupéry,* **Le Petit Prince**

Table A.1: NEI model abundances derived from *Chandra* and $XMM-Newton$ data.

Abun. ratio	This Thesis (NEI)	van der Heyden [34] (NEI)	LMC [81]
O/Si	0.12±0.16	0.45±0.08	0.61
Ne/Si	0.25±0.09	0.37±0.07	0.93
Mg/Si	0.20±0.08	0.25±0.06	1.03
S/Si	1.4±0.48	1.91±0.21	1.16
Ar/Si		2.56±0.64	0.54
Ca/Si		2.91±0.87	0.34
FeL/Si	0.55±0.1	0.52±0.14	1.16
FeK/Si		1.24±0.44	1.16

Table A.2: Shock model abundances derived from *Chandra* data, compared to abundances from van der Heyden [34] and theoretical predictions referenced therein.

Abun. ratio	This Thesis (shock)	van der Heyden (NEI)	Type Ia		Type II		LMC
			W7	WDD1	$12M_\odot$	$20M_\odot$	
O/Si	0.09	0.45±0.08	0.070	0.019	0.17	1.14	0.61
Ne/Si	0.16	0.37±0.07	0.005	0.001	0.13	1.08	0.93
Mg/Si	0.09	0.25±0.06	0.061	0.019	0.13	2.07	1.03
S/Si	3.02	1.91±0.21	1.074	1.167	1.63	0.5	1.16
Ar/Si	1.31	2.56±0.64	0.751	0.935	2.19	0.35	0.54
Ca/Si	0.82	2.91±0.87	0.891	1.382	1.75	0.42	0.34
FeL/Si	0.67	0.52±0.14	1.88	0.866	0.23	0.30	1.16
FeK/Si		1.24±0.44	1.88	0.866	0.23	0.30	1.16

Table A.3: Positions of radio sources at epoch 2000.90.

Source	Position (J2000)		Distance from
	Right Ascension	Declination	pulsar (arcmin)
PSR B1951+32	$19^{h}52^{m}58.^{s}2(1)$	$+32°52'41''(1)$	...
1	$19^{h}53^{m}17.^{s}80(1)$	$+32°52'09.''6(1)$	4.1
2	$19^{h}53^{m}16.^{s}36(1)$	$+32°48'46.''4(1)$	5.5
3	$19^{h}53^{m}15.^{s}63(1)$	$+32°59'38.''1(1)$	7.9
4	$19^{h}53^{m}25.^{s}41(1)$	$+32°58'12.''5(1)$	8.0
5	$19^{h}53^{m}13.^{s}41(1)$	$+33°01'21.''8(1)$	9.3
6	$19^{h}52^{m}15.^{s}79(1)$	$+32°49'35.''7(1)$	9.4
7	$19^{h}52^{m}15.^{s}64(1)$	$+32°49'39.''2(1)$	9.4

Values in parentheses indicate the uncertainty in the last digit.

Table A.4: Measured pulsar braking indices.

Pulsar	Associated SNR or Nebula	Braking Index	Reference
B0540-69	0540–69.3	1.81 ± 0.07	[102]
B0531+21	Crab Nebula	2.51 ± 0.01	[52]
B1509-58	G320.4–01.2	2.837 ± 0.001	[43]
B0833-45	Vela Nebula	1.4 ± 0.2	[51]
J1119-6127	none	2.91 ± 0.05	[10]

Table A.5: Initial period estimates for young pulsars.

Pulsar	Associated SNR or Nebula	Initial Period (ms)	Reference
J0537–6910	N 157B	< 14	[56]
B0531+21	Crab Nebula	19	[53]
B1951+32	CTB 80	27 ± 6	This thesis, [63]
B0540–69	0540–69.3	30 ± 8	[75]
J0205+6449	3C 58	60	[67]
J1811–1925	G11.2–0.3	62	[91, 44]
J1124–5916	G292.0+1.8	90	[11]

Table A.6: Young (< 1 *kyr*) Supernova Remnants in the Large Magellanic Cloud [37].

SNR	Age or Radius	SN Type
SN 1987A	8 yr	II
0540-69.3	1.5 pc	II
N157B	1.8 pc	(II)
N103B	3.0 pc	II?
0509-67.5	3.3 pc	Ia
0509-69.0	3.6 pc	Ia

Appendix B

Figures

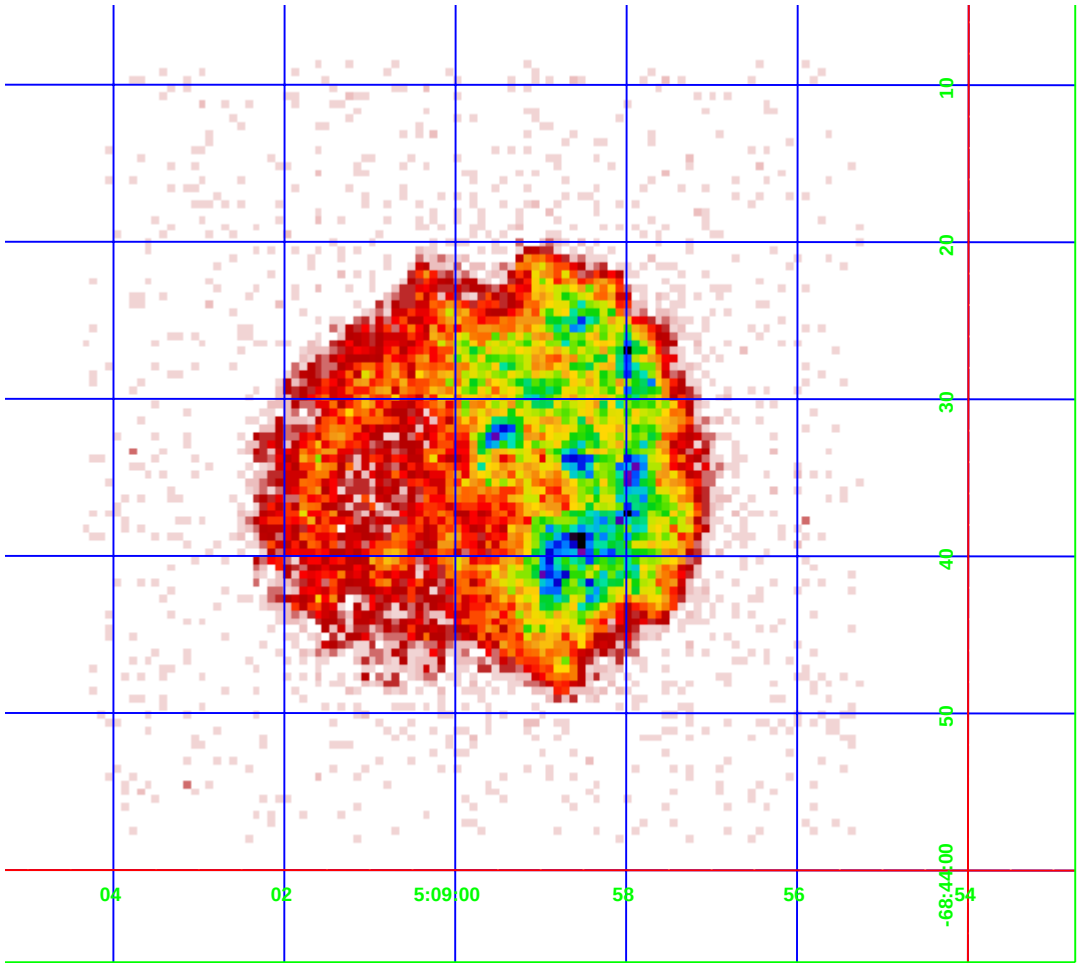

Figure B-1: *Chandra* ACIS image of SNR N103B ($0.4 - 10\ keV$).

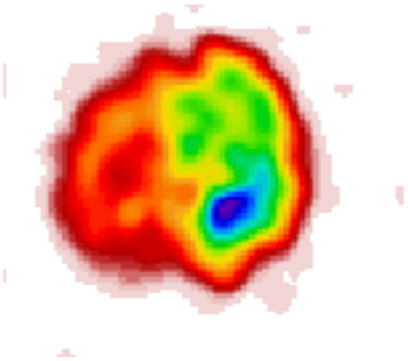

Figure B-2: *Chandra* ACIS zeroth-order image of [Ne X].

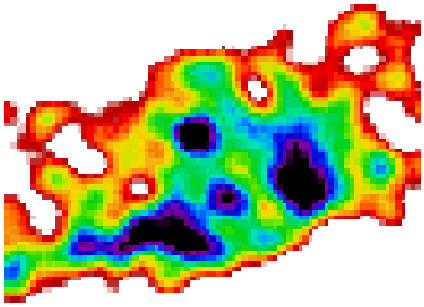

Figure B-3: *Chandra* HETG dispersed image of [Ne X].

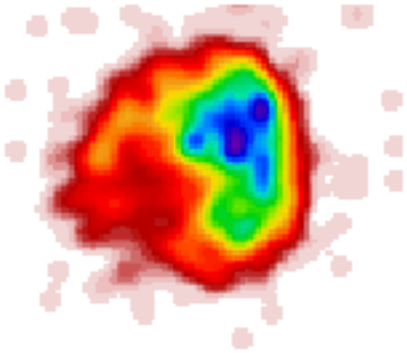

Figure B-4: *Chandra* ACIS zeroth-order image of [O VIII].

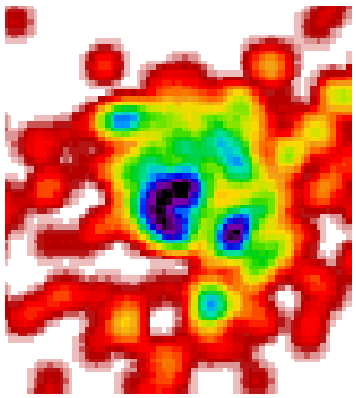

Figure B-5: *Chandra* HETG dispersed image of [O VIII].

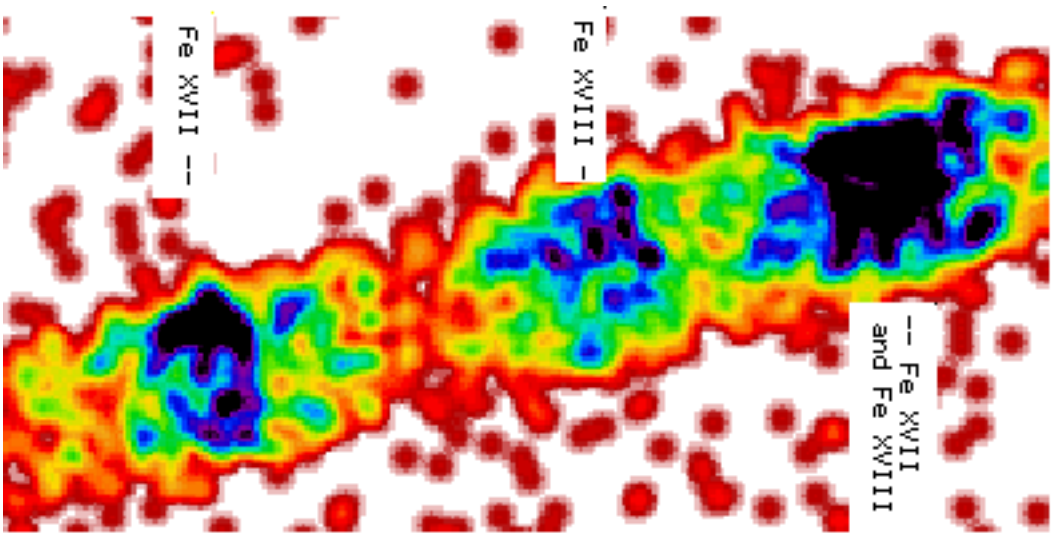

Figure B-6: *Chandra* HETG dispersed image of (from left to right) [Fe XVII] at ∼17 Å, [Fe XVIII] and [O VIII] at ∼16 Å, and [Fe XVII] and [Fe XVIII] at ∼15 Å.

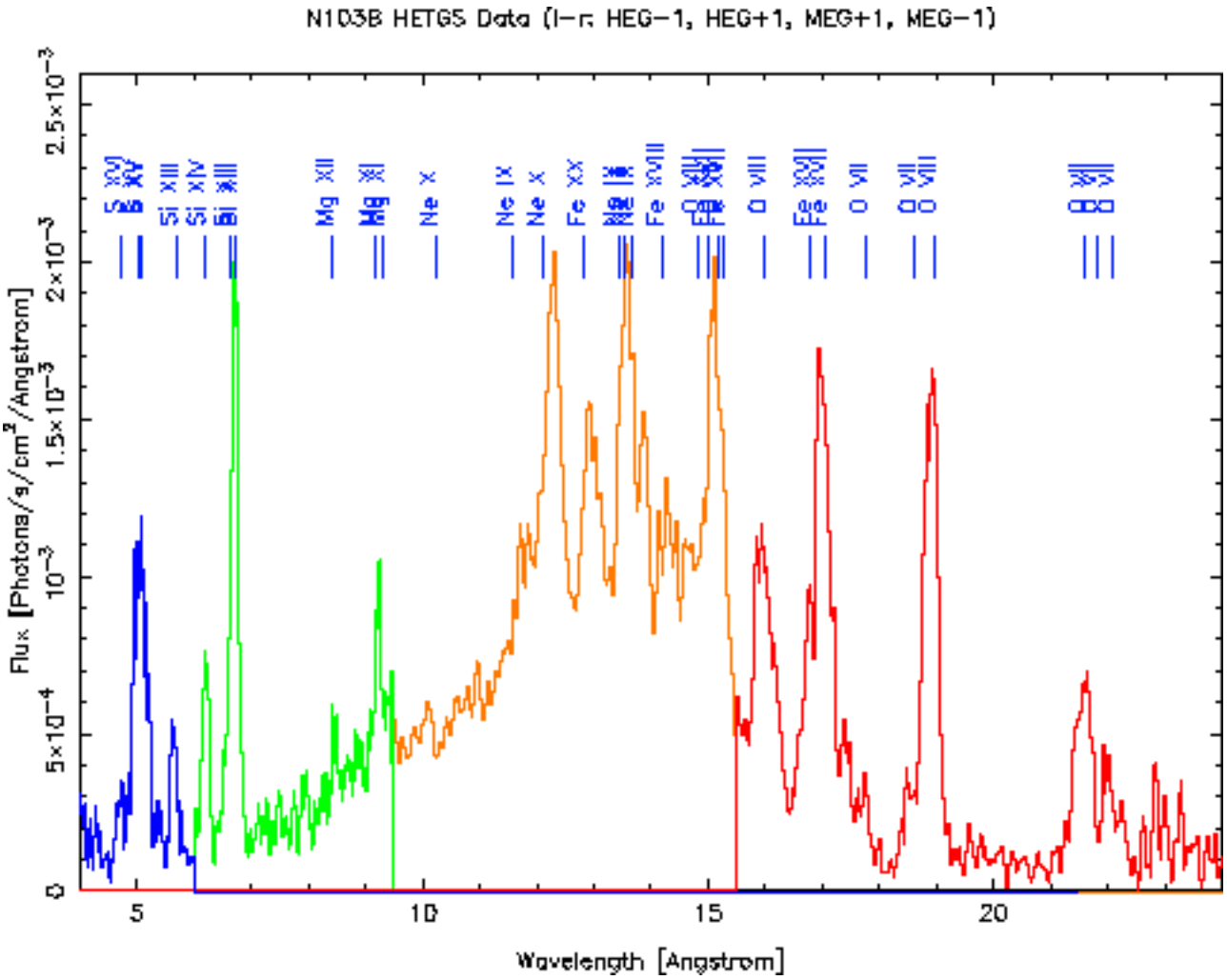

Figure B-7: Global *Chandra* HETG spectrum of SNR N103B.
The color coding indicates the source of spectral data (from left to right): HEG minus first, plus first, MEG plus first, and minus first orders.

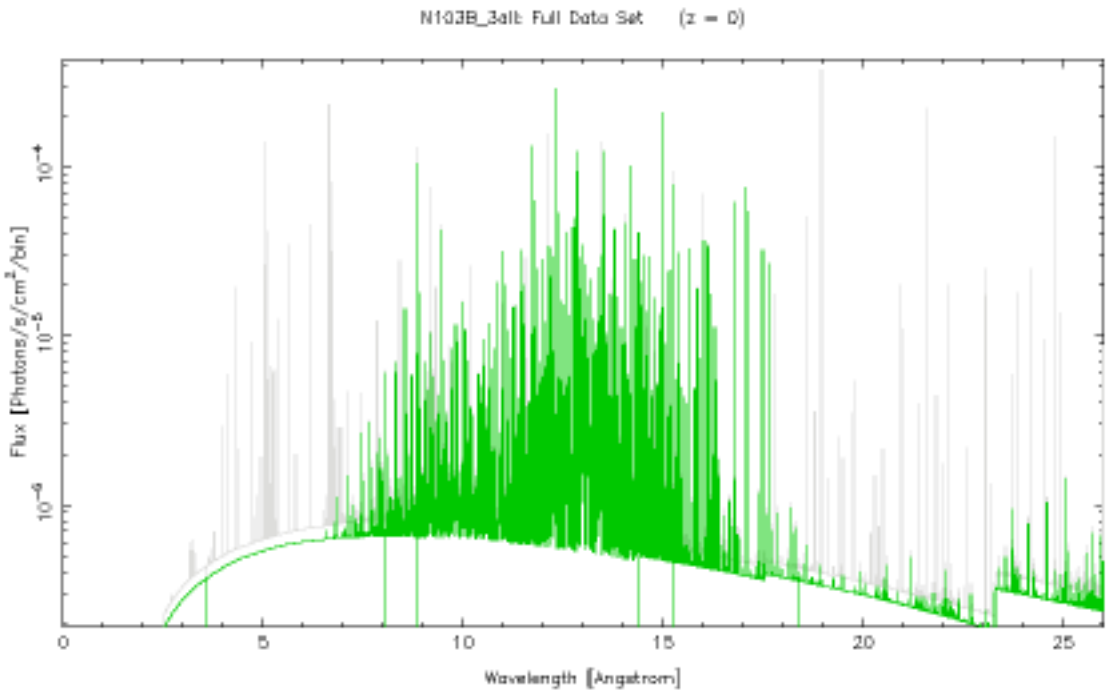

Figure B-8: The Iron Contribution to the global N103B spectrum.
The many emission lines in the global spectrum, in gray, and the large contribution of iron, in green, is readily appreciated.

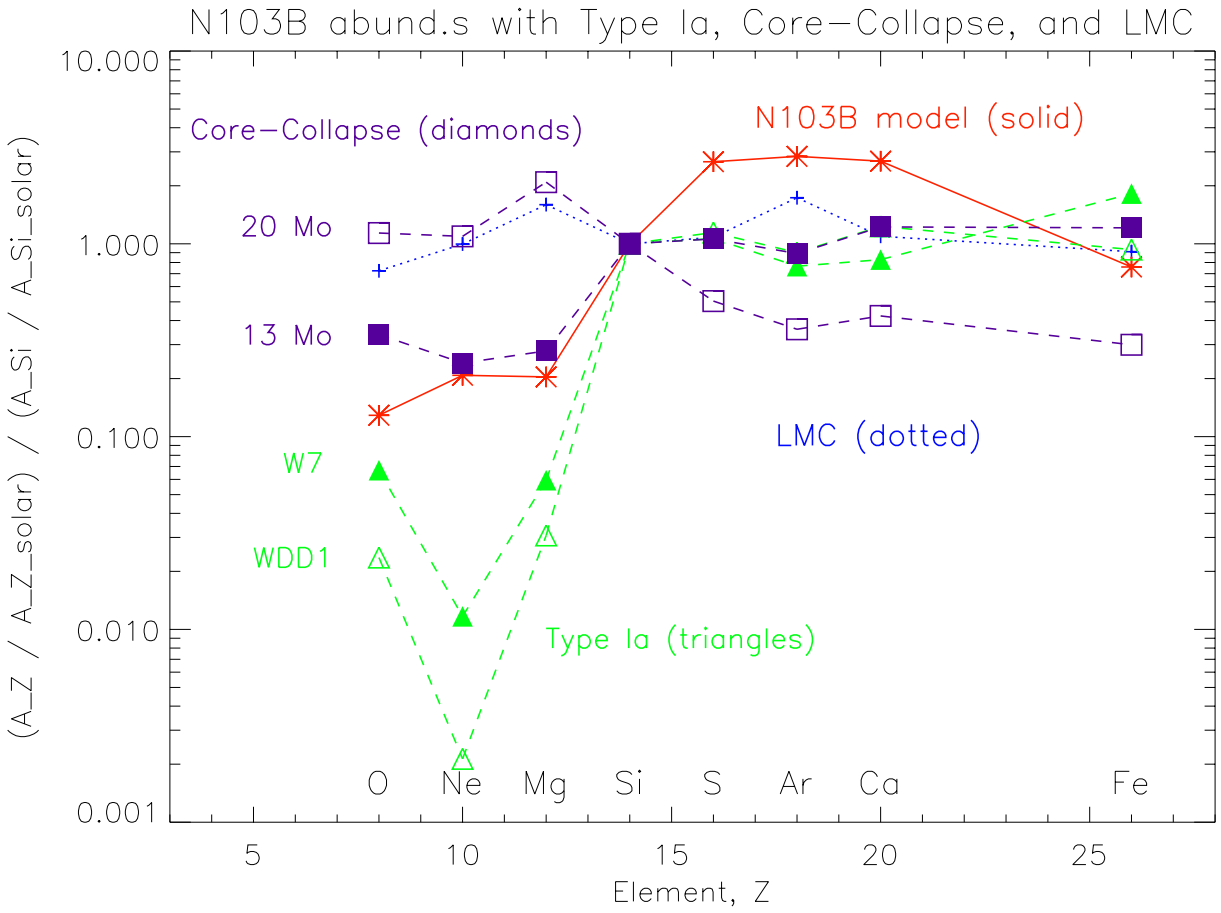

Figure B-9: Maximum N103B elemental abundaces consistent with our *Chandra* HETG spectra, compared to theoretical predictions [40, 89].

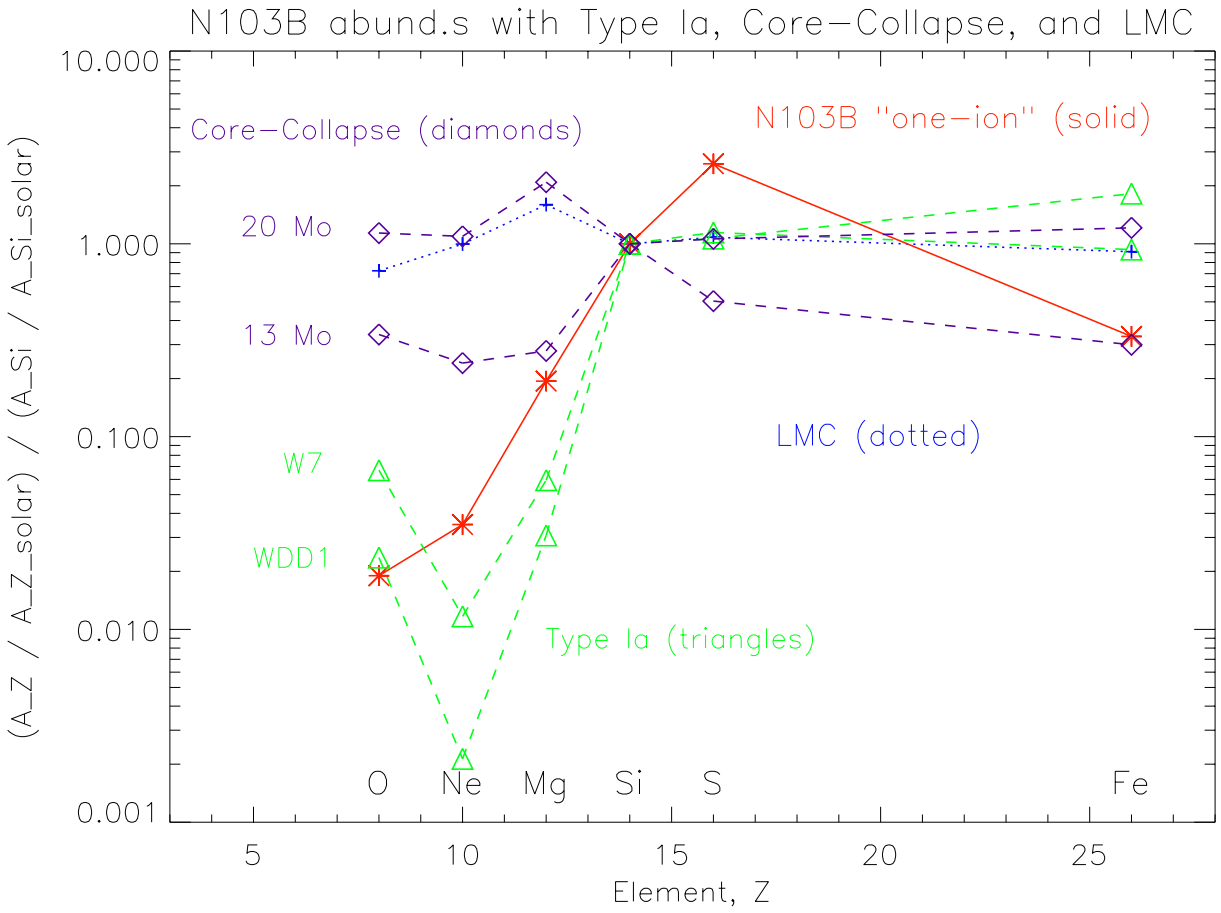

Figure B-10: Minimum N103B elemental abundaces consistent with our *Chandra* HETG spectra, compared to theoretical predictions [40, 89].

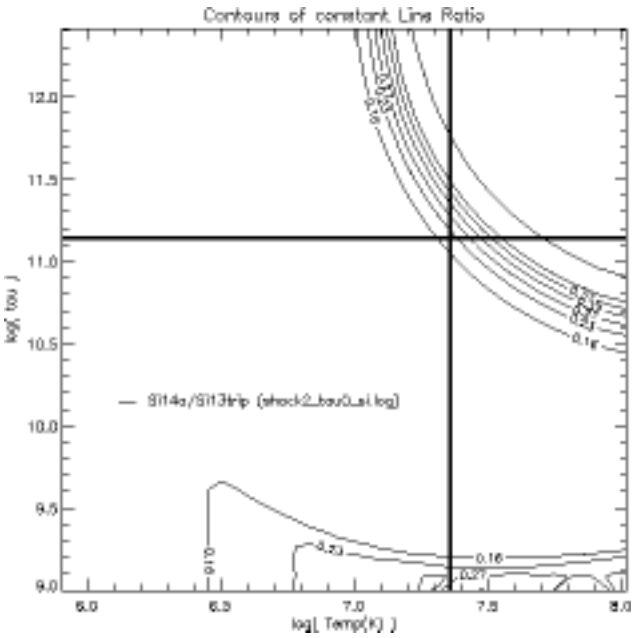

Figure B-11: Contours of constant Emission Line Flux Ratio for Si.
The cross marks the best fit shock model values of the silicon region: a temperature of 2.2 keV and an ionization age of 1.4×10^{11} $s\ cm^{-3}$.

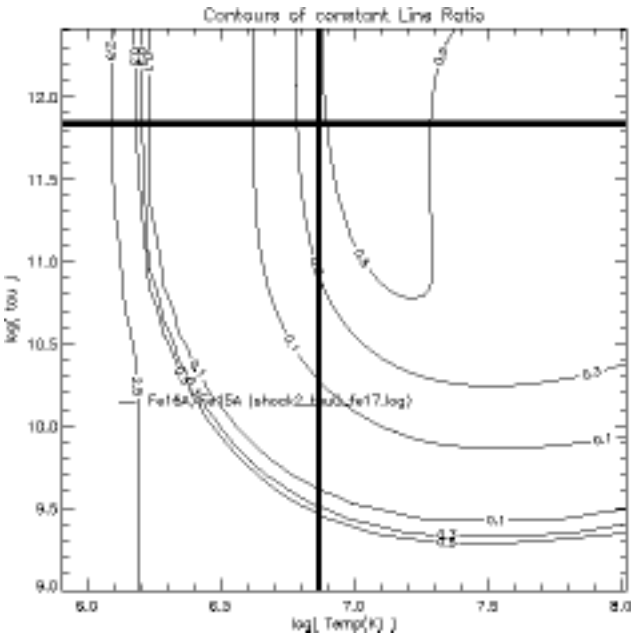

Figure B-12: Contours of constant Emission Line Flux Ratio for Fe.
The cross marks the best fit shock model values of the iron region: a temperature of 0.66 keV and an ionization age of 6.9×10^{11} $s\ cm^{-3}$.

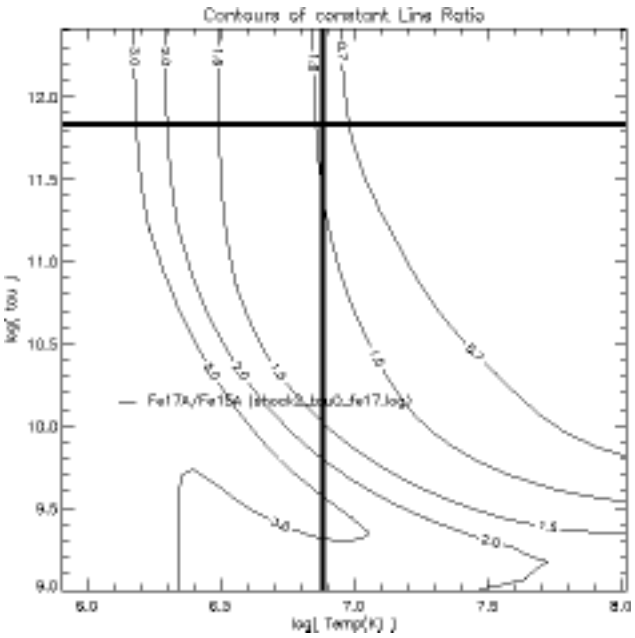

Figure B-13: Contours of constant Emission Line Flux Ratio for Fe.
The cross marks the best fit shock model values of the iron region: a temperature of 0.66 keV and an ionization age of 6.9×10^{11} $s\ cm^{-3}$.

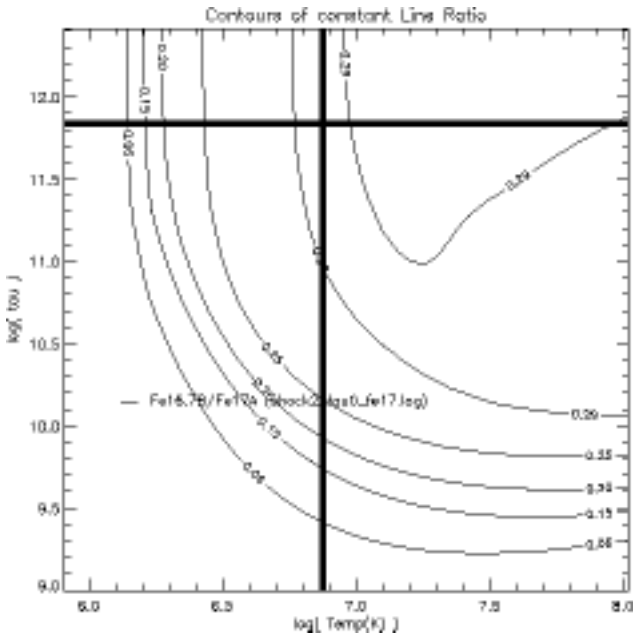

Figure B-14: Contours of constant Emission Line Flux Ratio for Fe.
The cross marks the best fit shock model values of the iron region: a temperature of 0.66 keV and an ionization age of 6.9×10^{11} $s\ cm^{-3}$.

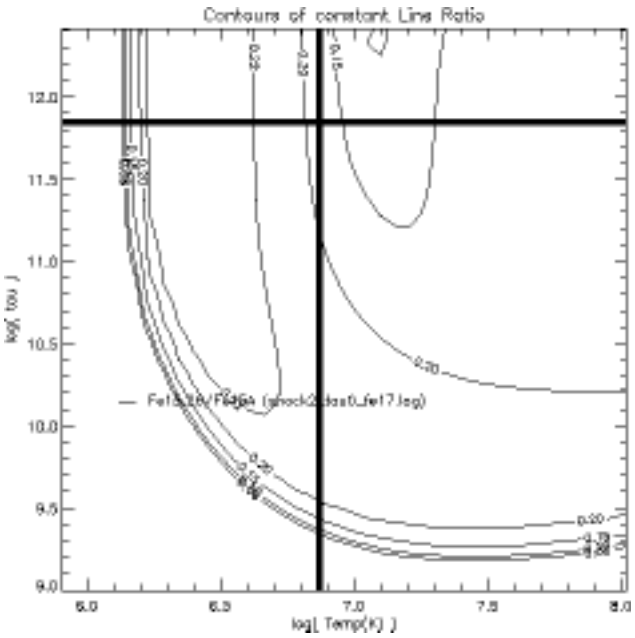

Figure B-15: Contours of constant Emission Line Flux Ratio for Fe.
The cross marks the best fit shock model values of the iron region: a temperature of 0.66 keV and an ionization age of 6.9×10^{11} $s\ cm^{-3}$.

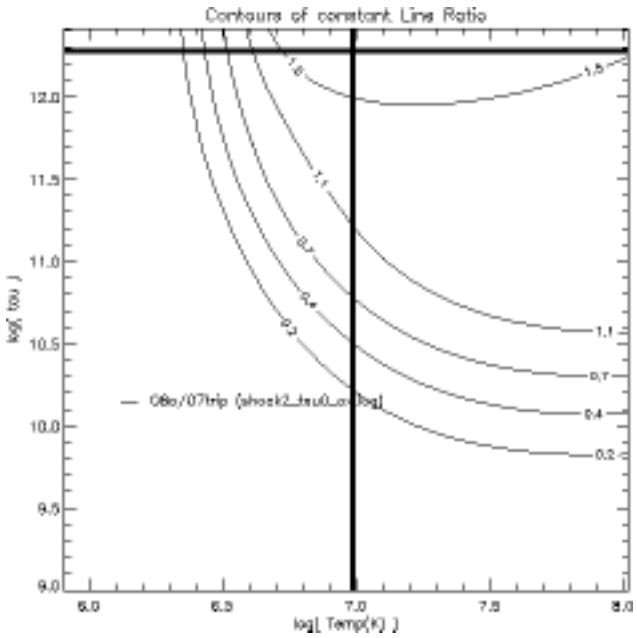

Figure B-16: Contours of constant Emission Line Flux Ratio for O.
The cross marks the best fit shock model values of the iron region: a temperature of 0.84 keV and an ionization age of 1.9×10^{11} $s\ cm^{-3}$.

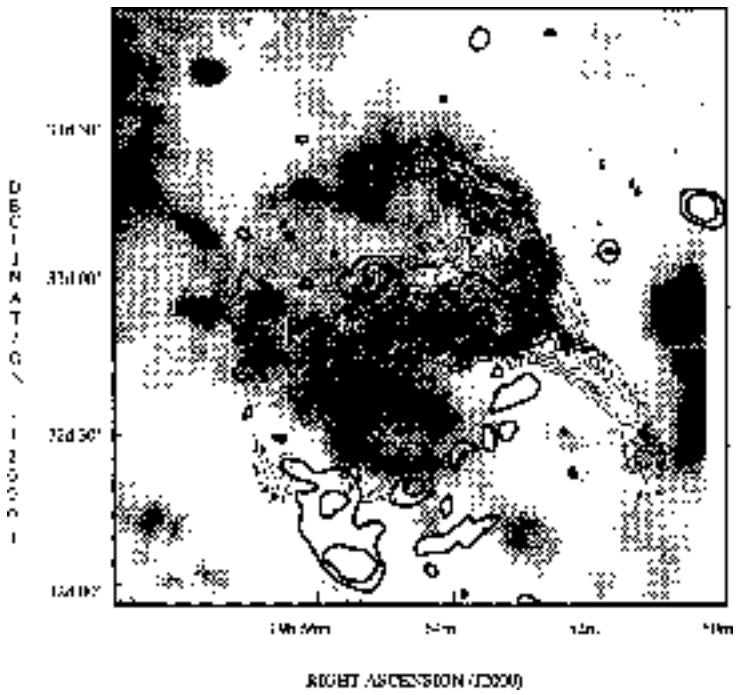

Figure B-17: The X-ray contours of CTB 80 in the $1 - 2.4\ keV$ band (*dark contours*) superimposed upon the brightness distribution of the 49 *cm* radio ridges (*light contours*) and the 1° diameter shell of infrared emission (*shaded regions*) [82].

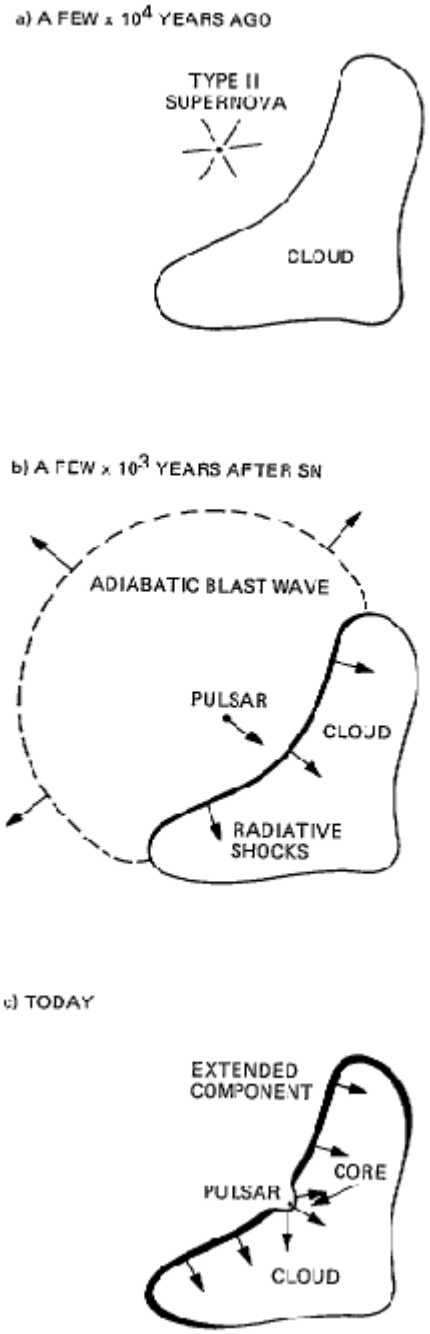

Figure B-18: Proposed evolution of CTB 80.

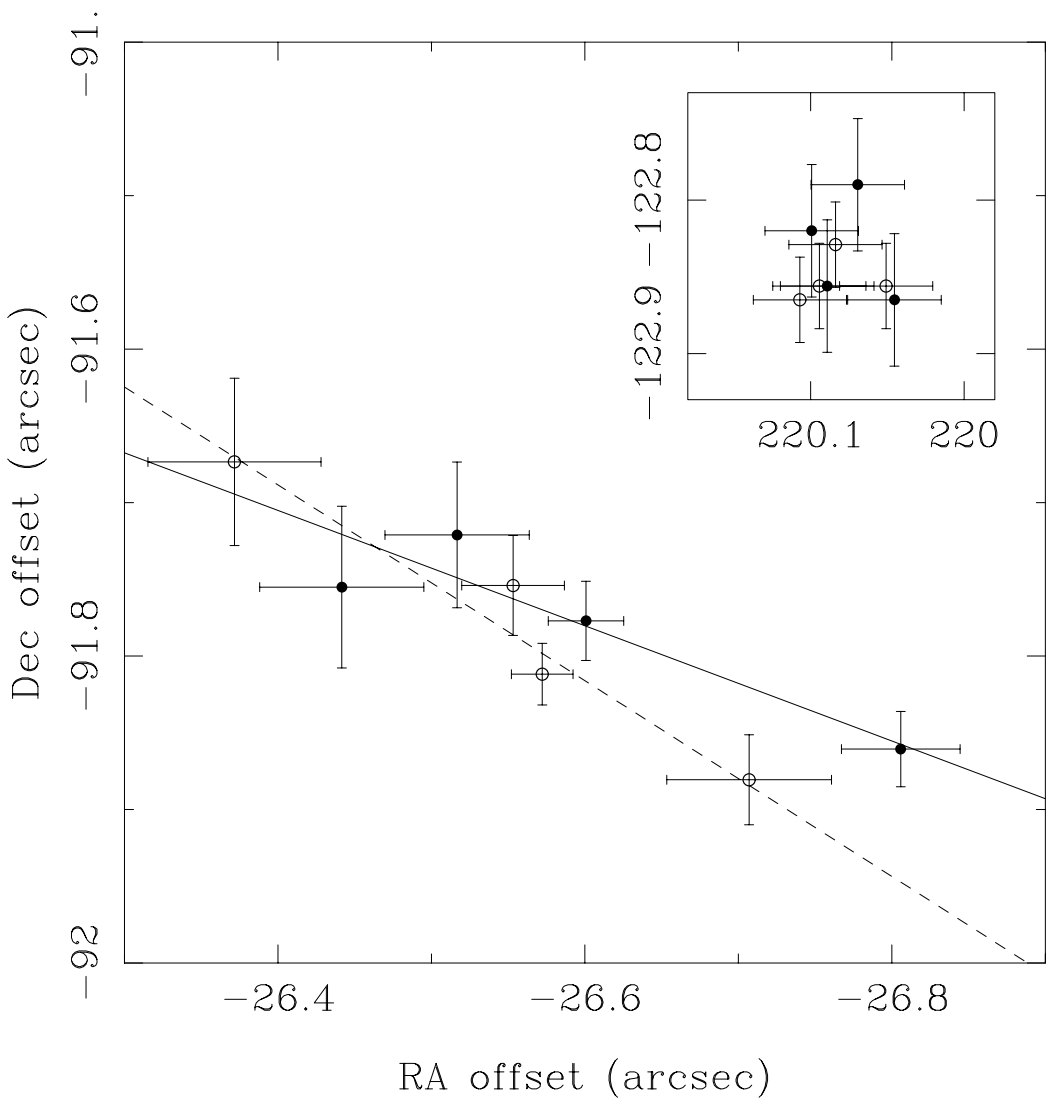

Figure B-19: Proper motion measurements of PSR B1951+32.
The data points show the offset of the pulsar from the mean reference position at four epochs, and the lines show the weighted best fit to these data. The solid circles and solid line correspond to 1385-MHz data, while the open circles and dashed line represent 1516/1652-MHz data. From left to right, the data points correspond to observations at epochs 1989.04, 1991.55, 1993.02 and 2000.90. The inset shows the position of source 1 at each epoch, plotted on the same scale and determined via the same process.

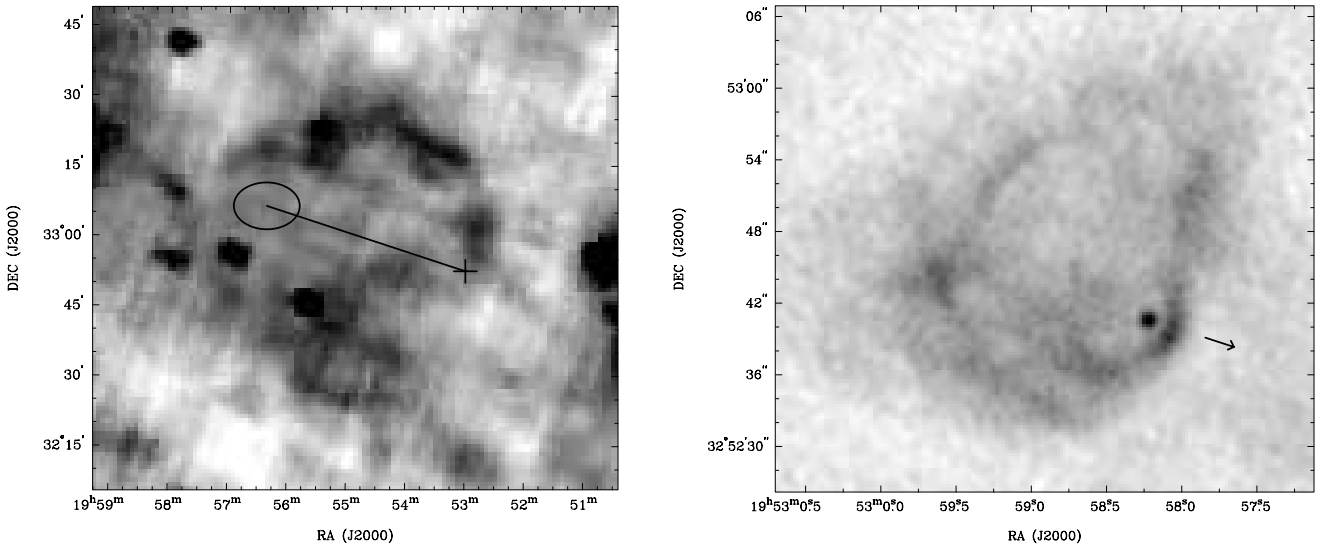

Figure B-20: SNR CTB 80 and PSR B1951+32.
The left panel presents an image of the *IRAS* 60/100 μm ratio in the region, showing the shell of CTB 80. The current position of PSR B1951+32 is marked by the "+" symbol, the direction along which it has traveled is indicated by the solid line, and its projected birthplace for an age of 107 *kyr* is marked by the 1σ ellipse. This birthplace, inferred from the pulsar's characteristic age, is strinkingly displaced from the geometrical center of the remnant.

In the right panel, we show a 1.5-GHz VLA image of the immediate vicinity of the pulsar, made from all baselines of our 1993-epoch data. PSR B1951+32 is the point-source to the south-west of center. The arrow indicates the pulsar's measured direction of motion, the length of the arrow corresponding to the distance traveled by the pulsar over 100 years.

Bibliography

[1] L. Angelini, N. E. White, A. N. Parmar, A. Smith, and M. A. Stevens. An EXOSAT observation of CTB 80. *Astrophysical Journal*, 330:L43, July 1988.

[2] P. E. Angerhofer, J. R. Mould, and A. S. Wilson. The central radio source in the peculiar supernova remnant CTB:80. *Astrophysical Journal*, 236:143, February 1980.

[3] P. E. Angerhofer, R. G. Strom, T. Velusamy, and M. R. Kundu. A multi-frequency study of CTB:80 with the Westerbork Synthesis Radio Telescope. *Astronomy and Astrophysics*, 94:313A, 1981.

[4] W. D. Arnett, D. N. Schramm, and J. W. Truran. On relative supernova rates and nucleosynthesis roles. *Astrophysical Journal*, 339:L25, April 1989.

[5] M. Bailes, R. N. Manchester, M. J. Kesteven, R. P. Norris, and J. Reynolds. The proper motion of the VELA pulsar. *Astrophysical Journal*, 343:L53, August 1989.

[6] R. H. Becker, D. J. Helfand, and A. E. Szymkowiak. An X-ray study of two Crablike supernova remnants - 3C 58 and CTB 80. *Astrophysical Journal*, 255:557, April 1982.

[7] S. van den Bergh and G. A. Tammann. Galactic and supergalactic supernova rates. *Annual Review of Astronomy and Astrophysics*, 29:363, 1991.

[8] W. P. Blair, R. A. Fesen, T. R. Rull, and R. P. Kirshner. An optical investigation of the peculiar supernova remnant CTB 80. *Astrophysical Journal*, 282:161, July 1984.

[9] K. J. Borkowski, W. J. Lyerly, and S. P. Reynolds. Supernova remnants in the Sedov expansion phase: Thermal X-ray emission. *Astrophysical Journal*, 548:820, February 2001.

[10] F. Camilo, V. M. Kaspi, A. G. Lyne, R. N. Manchester, J. F. Bell, N. D'Amico, N. P. F. McKay, and F. Crawford. Discovery of two high magnetic field radio pulsars. *Astrophysical Journal*, 541:367, September 2000.

[11] F. Camilo, R. N. Manchester, B. M. Gaensler, D. R. Lorimer, and J. Sarkissian. PSR J1124-5916: Discovery of a young energetic pulsar in the supernova remnant G292.0+1.8. *Astrophysical Journal*, 567:L71, March 2002.

[12] C. R. Canizares. *et al.* in preparation.

[13] C. R. Canizares, D. P. Huenemoerder, D. S. Davis, D. Dewey, K. A. Flanagan, J. Houck, T. H. Markert, H. L. Marshall, M. L. Schattenburg, N. S. Schulz, M. Wise, J. J. Drake, and N. S. Brickhouse. High-resolution X-ray spectra of capella: Initial results from the Chandra High-Energy Transmission Grating Spectrometer. *Astrophysical Journal*, 539:L41, August 2000.

[14] G. Chanmugan. Magnetic fields of pulsars. *Astrophysical Journal*, 182:L39, May 1973.

[15] R. A. Chevalier and R. T. Emmering. Are pulsars born as slow rotators? *Astrophysical Journal*, 304:140, May 1986.

[16] Y.-H. Chu and R. C. Kennicutt Jr. Environments and populations of supernova remnants in the Large Magellanic Cloud. *Astronomical Journal*, 96(6):1874, December 1988.

[17] I. J. Danziger and E. M. Leibowitz. Optical spectrophotometric study of supernova remnants in the Large Magellanic Cloud. *Royal Astronomical Society, Monthly Notices*, 216:365, September 1985.

[18] D. Dewey. Extended source analysis for grating spectrometers. In G. Branduardi-Raymont, editor, *High Resolution X-ray Spectroscopy with XMM-Newton and Chandra*, Proceedings of the international workshop held at the Mullard Space Science Laboratory of University College London, Holmbury St Mary, Dorking, Surrey, UK, October 24 - 25, 2002, page E14. to be published electronically at **http://www.mssl.ucl.ac.uk/ gbr/rgs_workshop/papers/**, 2002.

[19] J. R. Dickel and D. K. Milne. Radio properties of three young supernova remnants in the Large Magellanic Cloud. *Astronomical Journal*, 109(1669):200, January 1995.

[20] R. C. Dohm-Palmer and T. W. Jones. Young supernova remnants in nonuniform media. *Astrophysical Journal*, 471:279, November 1996.

[21] D. Downes. *Radio Sources in the Galactic Plane*. PhD thesis, Harvard University, 1970.

[22] R. A. Fesen, J. M. Saken, and J. M. Shull. Interaction between high-velocity pulsar in CTB 80 and an infrared emission shell. *Nature*, 334:229, July 1988.

[23] M. Fich, L. Blitz, and A. A. Stark. The rotation curve of the Milky Way to 2 R(0). *Astrophysical Journal*, 342:272, July 1989.

[24] K. A. Flanagan. *et al.* 2003, in preparation.

[25] R. S. Foster, D. C. Backer, and A. Wolszczan. Timing properties of PSR 1951 +32 in the CTB 80 supernova remnant. *Astrophysical Journal*, 356:243, June 1990.

[26] R. S. Foster, A. G. Lyne, S. L. Shemar, and D. C. Backer. A six year timing solution for PSR B1951 + 32. *Astrophysical Journal*, 108(1):175, 1989.

[27] D. A. Frail, W. M. Goss, and J. B. Z. Whiteoak. The radio lifetime of supernova remnants and the distribution of pulsar velocities at birth. *Astrophysical Journal*, 437(2):781, 1994.

[28] A. S. Fruchter, J. H. Taylor, D. C. Backer, T. R. Clifton, and R. S. Foster. Timing and scintillation observations of the fast pulsar in CTB 80. *Nature*, 331:53, January 1988.

[29] B. M. Gaensler and D. A. Frail. A large age for the pulsar B1757-24 from an upper limit on its proper motion. *Nature*, 406:158, 2000.

[30] P. Goldreich and W. H. Julian. Pulsar electrodynamics. *Astrophysical Journal*, 157:869, August 1969.

[31] D. A. Green. A catalogue of Galactic supernovae remnants. In R. McCray and Z. Wang, editors, *Supernovae and other Supernova Remnants*, Proceedings of the IAU Colloquium 145. IAU, Cambridge University Press, May 1994.

[32] V. V. Gvaramadze. On neutron star/supernova remnant associations. In P. O. Slane and B. M. Gaensler, editors, *Neutron Stars in Supernova Remnants*, volume 271 of *Astronomical Society of the Pacific Conference Series*, pages 23–26, San Franscisco, 2002. ASP, Astronomical Society of the Pacific.

[33] J. J. Hester and S. R. Kulkarni. The origin and energetics of CTB 80. *Astrophysical Journal*, 331:L121, August 1988.

[34] K. J. van der Heyden, E. Behar, J. Vink, A. P. Rasmussen, J. S. Kaastra, J. A. M. Bleeker, S. M. Kahn, and R. Mewe. High-resolution X-ray imaging and spectroscopy of N 103B. *Astronomy and Astrophysics*, 392:955, September 2002.

[35] B. Hnatyk and O. Petruk. Evolution of supernova remnants in the interstellar medium with a large-scale density gradient. I. General properties of the morphological evolution and X-ray emission. *Astronomy and Astrophysics*, 344:295, April 1999.

[36] J. P. Hughes. Young supernova remnants in the Magellanic Clouds. In S. S. Holt and U. Hwang, editors, *Young Supernova Remnants: Eleventh Astrophysics Conference*, volume 565 of *AIP Conference Proceedings*, pages 419–428. AIP, American Institute of Physics, 2001.

[37] J. P. Hughes, I. Hayashi, D. J. Helfand, U. Hwang, M. Itoh, R. Kirshner, K. Koyama, T. Markert, H. Tsunemi, and J. Woo. *ASCA* observations of the Large Magellanic Cloud supernova remnant sample: Typing supernovae from their remnants. *Astrophysical Journal*, 444(2):L81, May 1995.

[38] U. Hwang, R. Petre, E. Gotthelf, J. Hughes, and J. Keohane. X-ray spectroscopy of the supernova remnant N103B. In Y.-H. Chu, N. Suntzeff, J. Hesser, and D. Bohlender, editors, *New Views of the Magellanic Clouds*, volume 190 of *IAU Symposium*, page 141. IAU, 1999.

[39] U. Hwang, R. Petre, and J. P. Hughes. The X-ray line emission from the supernova remnant W49B. *Astrophysical Journal*, 532:970, April 2000.

[40] K. Iwamoto, F. Brachwitz, K. Nomoto, N. Kishimoto, H. Umeda, W. R. Hix, and F.-K. Thielemann. Nucleosynthesis in Chandrasekhar mass models for Type IA supernovae and constraints on progenitor systems and burning-front propagation. *Astrophysical Journal Supplement Series*, 125:439, December 1999.

[41] J. S. Kaastra. An X-ray spectral code for optically thin plasmas. *SRON-Leiden Report*, update version 2.0, 1992.

[42] V. M. Kaspi, E. V. Gotthelf, B. M. Gaensler, and M. Lyutikov. X-ray detection of pulsar PSR b1757-24 and its nebular tail. *Astrophysical Journal*, 562:L163, December 2001.

[43] V. M. Kaspi, R. N. Manchester, B. Siegman, S. Johnston, and A. G. Lyne. On the spin-down of PSR b1509-58. *Astrophysical Journal*, 422(2):L83, February 1994.

[44] V. M. Kaspi, M. E. Roberts, G. Vasisht, E. V. Gotthelf, M. Pivovaroff, and N. Kawai. Chandra X-ray observations of G11.2-0.3: Implications for pulsar ages. *Astrophysical Journal*, 560:371, October 2001.

[45] B. C. Koo, W. T. Reach, C. Heiles, R. A. Fesen, and J. M. Shull. Detection of an expanding H I shell in the old supernova remnant CTB 80. *Astrophysical Journal*, 364:178, November 1990.

[46] S. R. Kulkarni, T. C. Clifton, D. C. Backer, R. S. Foster, and A. S. Fruchter. A fast pulsar in radio nebula CTB 80. *Nature*, 331:50, January 1988.

[47] W. Kundt and Hsiang-Kuang Chang. Pulsar nebulae. *Astrophysics and Space Science*, 193(1):145, July 1992.

[48] K. T. Lewis, D. N. Burrows, G. P. Garmire, J. A. Nousek, J. P. Hughes, and P. Slane. The small scale structure of N103B: Nature or nurture? In E. M. Schlegel and Saeqa Dil Vrtilek., editors, *The High Energy Universe at Sharp Focus: Chandra Science*, volume 262 of *ASP Conference Proceedings*, page 323. Astronomical Society of the Pacific, San Francisco: ASP, 2002.

[49] K. T. Lewis, D. N. Burrows, J. P. hughes, P. O. Slane, G. P. Garmire, and J. A. Nousek. The radial structure of SNR N103B. arXiv:astro-ph/0209280v1, 13 September 2002.

[50] K. S. Long, D. J. Helfand, and D. A. Grabelsky. A soft X-ray study of the Large Magellanic Clouds. *Astrophysical Journal*, 248:925, September 1981.

[51] A. G. Lyne, R. S. Pritchard, F. Graham-Smith, and F. Camilo. Very low braking index for the VELA pulsar. *Nature*, 381:497, 1996.

[52] A. G. Lyne, R. S. Pritchard, and F. G. Smith. Crab pulsar timing 1982-87. *Royal Astronomical Society, Monthly Notices*, 233:667, August 1988.

[53] R. N. Manchester and J. H. Taylor. *Pulsars*. San Fransciso: Freeman, 1977.

[54] F. Mantovani, W. Reich, C. J. Salter, and P. Tomasi. Further observations of radio sources from the BG survey. III - CTB 80. *Astronomy and Astrophysics*, 145(1):50, April 1985.

[55] T. H. Markert, D. R. Canizares, D. Dewey, M. McGuirk, C. S. Pak, and M. L. Schattenburg. High-Energy transmission Grating Spectrometer for the Advanced X-ray Astrophysics Facility (AXAF). In Oswald H. Siegmund and John V. Vallerga, editors, *EUV, X-Ray, and Gamma-Ray Instrumentation for Astronomy V*, volume 2280 of *Proceedings SPIE*, pages 168–180. SPIE, The International Society for Optical Engineering, September 1994.

[56] F. E. Marshall, E. V. Gotthelf, W. W. Zhang, J. Middleditch, and Q. D. Wang. Discovery of an ultrafast X-ray pulsar in the supernova remnant N157B. *Astrophysical Journal*, 499:L179, June 1998.

[57] D. S. Mathewson and J. N. Clarke. Supernova remants in the Large Magellanic Clouds. *Astrophysical Journal*, 180:725, March 1973.

[58] D. S. Mathewson, V. L. Ford, M. A. Dopita, I. R. Tuohy, K. S. Long, and D. J. Helfand. Supernova remnants in the Magellanic Clouds. *Astrophysical Journal Supplement Series*, 51:345, April 1983.

[59] D. S. Mathewson, V. L. Ford, M. A. Dopita, I. R. Tuohy, B. Y. Mills, and A. J. Turtle. Supernova remnants in the Magellanic Clouds. *Astrophysical Journal Supplement Series*, 55:189, June 1984.

[60] D. S. Mathewson, V. L. Ford, I. R. Tuohy, B. Y. Mills, A. J. Turtle, and D. J. Helfand. Supernova remnants in the Magellanic Clouds. III. *Astrophysical Journal Supplement Series*, 58:197, June 1985.

[61] F. Matteucci. The role of SNs in the chemical evolution of galaxies. In I. J. Danziger and Kurt Kjär, editors, *Supernova 1987A and other supernovae*, ESO Conference and Workshop Proceedings, page 703. ESO/EPIC, Garching: European Southern Observatory (ESO), 1991.

[62] R. S. McGary, W. F. Brisken, A. S. Fruchter, W. M. Goss, and S. E. Thorsett. Proper-motion measurements with the VLA. I. Wide-field imaging and pulse-gating techniques. *Astronomical Journal*, 121:1192, 2001.

[63] J. M. Migliazzo, B. M. Gaensler, D. C. Backer, B. W. Stappers, E. van der Swaluw, and R. G. Strom. Proper-motion measurements of pulsar B1951+32 in the supernova remnant CTB 80. *Astrophysical Journal*, 567:L141–144, March 2002.

[64] B. Y. Mills, A. J. Turtle, A. G. Little, and J. M. Durdin. A new look at radio supernova remnants. *Australian Journal of Physics*, 37(3):321, 1984.

[65] D. K. Milne, J. L. Caswell, and R. F. Haynes. Supernova remnants in the Large Magellanic Cloud. *Royal Astronomical Society, Monthly Notices*, 191:469, May 1980.

[66] R. Morrison and D. McCammon. Interstellar photoelectric absorption cross sections, 0.03-10 keV. *Astrophysical Journal*, 270:119, July 1983.

[67] S. S. Murray, P. O. Slane, F. D. Seward, S. M. Ransom, and B. M. Gaensler. Discovery of X-ray pulsations from the compact central source in the supernova remnant 3C 58. *Astrophysical Journal*, 568:226, March 2002.

[68] H Ögelman and R. Buccheri. Soft X-ray imaging observations of the 39 millisecond pulsar PSR 1951 +32. *Astronomy and Astrophysics*, 186(1–2):L17, November 1987.

[69] J. P. Ostriker and J. E. Gunn. On the nature of pulsars. I. theory. *Astrophysical Journal*, 157:1395, September 1969.

[70] F. Pacini. Energy emission from a neutron star. *Nature*, 216:567, November 1967.

[71] F. Pacini. Magnetic dipole radiation from pulsars. *Nature*, 221:454, February 1968.

[72] B. E. J. Pagel, M. G. Edmunds, R. A. E. Fosbury, and B. L. Webster. A survey of chemical compositions of H II regions in the Magellanic Cloud. *Royal Astronomical Society, Monthly Notices*, 184:569, August 1978.

[73] P. V. Ramanamurthy, D. L. Bertsch, B. L. Dingus, J. A. Esposito, J. M. Fierro, C. E. Fichtel, S. D. Hunter, G. Kanbach, D. A Kniffen, Y. C. Lin, A. G. Lyne, J. R. Mattox, H. A. Mayer-Hasselwander, M. Merck, P. F. Michelson, C. von Montigny, R. Mukherjee, P. L. Nolan, and D. J. Thompson. EGRET detection of pulsed gamma radiation from PSR 1951 +32. *Astrophysical Journal*, 447:L109, July 1995.

[74] J. C. Raymond and B. W. Smith. Soft X-ray spectrum of a hot plasma. *Astrophysical Journal Supplement Series*, 35:419, December 1977.

[75] S. P. Reynolds. An evolutionary history for the Crablike, pulsar-powered supernova remnant 0540-69.3. *Astrophysical Journal*, 291:152, April 1985.

[76] S. P. Reynolds. Models of synchrotron X-rays from shell supernova remnants. *Astrophysical Journal*, 493:375, January 1998.

[77] S. P. Reynolds and J. W. Keokane. Maximum energies of shock-accelerated electrons in young shell supernova remnants. *Astrophysical Journal*, 525:368, November 1999.

[78] M. Rozyczka, G. Tenorio-Tagle, J. Franco, and P. Bodenheimer. On the evolution of supernova remnants. III - Off-centred supernova explosions in preexisting wind-driven bubbles. *Royal Astronomical Society, Monthly Notices*, 261(3):674, April 1993.

[79] S. C. Russell and M. S. Bessell. Abundances of the heavy elements in the Magellanic Clouds. I - Metal abundances of F-type supergiants. *Astrophysical Journal*, 70:865, August 1989.

[80] S. C. Russell and M. A. Dopita. Abundances of the heavy elements in the Magellanic Clouds. II - H II regions and supernova remnants. *Astrophysical Journal Supplement Series*, 74:93, September 1990.

[81] S. C. Russell and M. A. Dopita. Abundances of the heavy elements in the Magellanic Clouds. III - Interpretation of results. *Astrophysical Journal*, 384:508, January 1992.

[82] S. Safi-Harb and H. Ögelman. ROSAT observations of the unusual supernova remnant CTB 80 containing the pulsar PSR 1951 + 32. *Astrophysical Journal*, 439:722, 1995.

[83] R. J. Sault, P. J. Teuben, and M. C. H. Wright. A retrospective view of Miriad. In R. Shaw, H. E. Payne, and J. J. E. Hayes, editors, *Astronomical Data Analysis Software and Systems IV*, volume 77 of *Astronomical Society of the Pacific Conference Series*, pages 433–436, San Franscisco, 1995. Astronomical Society of the Pacific.

[84] J. M. Shull, R. A. Fesen, and J. M. Saken. Pulsar reenergization of old supernova remnant shells. *Astrophysical Journal*, 346:860, November 1989.

[85] K. P. Singh, N. J. Westergaard, H. W. Schnopper, and D. J. Helfand. X-ray observations of the supernova remnant N103B in the Large Magellanic Cloud. *Astrophysical Journal*, 322:80, November 1987.

[86] R. G. Strom. Pulsar-like emission from the supernova remnant CTB 80. *Astrophysical Journal*, 319:L103, August 1987.

[87] R. G. Strom, P. E. Angerhofer, and J. R. Dickel. A radio study of the flat spectrum component in CTB 80. *Astronomy and Astrophysics*, 139(1):43, October 1984.

[88] R. G. Strom and B. W. Stappers. Supernova remnant CTB 80 and PSR 1951+32. In M. Kramer, N. Wex, and N. Wielebinski, editors, *Pulsar Astronomy - 2000 and Beyond*, ASP Conference Series, Vol. 202; Proceedings of the 177th Colloquium of the IAU held in Bonn, Germany, page 509, San Francisco, August–September 1999. Astronomical Society of the Pacific.

[89] F.-K. Thielemann, K. Nomoto, and M.-A. Hashimoto. Core-collapse supernovae and their ejecta. *Astrophysical Journal*, 460:408, March 1996.

[90] R. J. Thompson, Jr., and F. A. Cordova. Revised proper-motion results for the soft X-ray-emitting radio pulsar PSR 0656+14. *Astrophysical Journal*, 421(1):L13, 1994.

[91] K. Torii, H. Tsunemi, T. Dotani, K. Mitsuda, N. Kawai, K. Kinugasa, Y. Saito, and S. Shibata. Spin-down of the 65 millisecond X-ray pulsar in the supernova remnant G11.2-0.3. *Astrophysical Journal*, 523:L69, September 1999.

[92] L. K. Townsley, P. S. Broos, G. P. Garmire, and J. A. Nousek. Mitigating charge transfer inefficiency in the Chandra X-Ray Observatory Advanced CCD Imaging Spectrometer. *Astrophysical Journal*, 534:L139, May 2000.

[93] T. Tsujimoto, K. Nomoto, Y. Yoshii, H. Hashimoto, S. Yanagida, and F. K. Thielemann. Relative frequencies of type Ia and type II supernovae in the chemical evolution of the Galaxy, LMC and SMC. *Royal Astronomical Society, Monthly Notices*, 277:945, December 1995.

[94] I. R. Tuohy, M. A. Dopita, D. S. Mathewson, K. S. Long, and D. J. Helfand. Optical identification of Balmer-dominated supernova remnants in the Large Magellanic Cloud. *Astrophysical Journal*, 261:473, October 1982.

[95] T. Velusamy and M. R. Kundu. Observations of intensity and linear polarization in supernova remnants at 11 cm wavelength. *Astronomy and Astrophysics*, 32:375, 1974.

[96] T. Velusamy, M. R. Kundu, and R. H. Becker. Observations of intensity and linear polarization of CTB 80 at 6 and 2.8 cm. *Astronomy and Astrophysics*, 51:21, 1976.

[97] M. Vivekanand and R. Narayan. A new look at pulsar statistics - Birthrate and evidence for injection. *Journal of Astrophysics and Astronomy*, 2:315, September 1981.

[98] Z. R. Wang and F. D. Seward. An X-ray investigation of the unusual supernova remnant CTB 80. *Astrophysical Journal*, 285:607, October 1984.

[99] K. W. Weiler. Plerions, regular and deluxe. In M. Kafaos and R. B. C. Henry, editors, *The Crab Nebula and related supernova remnants*, volume A86-41101 19-90 of *Proceedings of the Workshop, Fairfax, Virginia, Oct. 11,12, 1984*, pages 227–240, Cambridge and New York, 1985. Cambridge University Press.

[100] B. E. Westerlund. The Magellanic Clouds - Their evolution, structure and composition. *Astronomy and Astrophysics Review*, 2(1):29, 1990.

[101] M. J. Whitehead, J. Meaburn, and C. A. Clayton. Optical observations of the morphology and kinematics of the compact core of the peculiar supernova remnant CTB 80. *Royal Astronomical Society, Monthly Notices*, 237:1109, April 1989.

[102] W. Zhang, F. E. Marshall, E. V. Gotthelf, J. Middleditch, and Q. D. Wang. A phase-connected braking index measurement for the Large Magellanic Cloud pulsar PSR B0540-69. *Astrophysical Journal*, 554:L177, June 2001.